PHYSICAL REVIEW B VOLUME 38, NUMBER 11 15 OCTOBER 1988-I

Phonon radiative heat transfer and surface scattering

Tom Klitsner, J. E. VanCleve, Henry E. Fischer, and R. O. Pohl
Laboratory of Atomic and Solid State Physics, Cornell University, Ithaca, New York 14853-2501

(Received 21 December 1987)

We have performed thermal-conductance measurements on polished single crystals of pure silicon in the low-temperature boundary-scattering regime. Our data show that the thermal conductance depends not only on the sample size, but also on the size and spacing of the thermometers used to measure the temperature gradient along the crystal. We have analyzed the heat transport in terms of phonon blackbody radiation subject to surface scattering from the attached thermometers and from the free surfaces of the crystal. We have made this analysis quantitative by using Monte Carlo techniques, and have calculated the magnitude of both surface scattering effects. We show that thermal-conductance measurements provide a very sensitive and precise technique for studying diffuse phonon scattering at crystal surfaces, and find that our highly polished and clean silicon surfaces will specularly reflect more than 99% of the incident phonons below 1 K, temperatures which correspond to dominant phonon frequencies less than 90 GHz.

I. INTRODUCTION

In pure dielectric single crystals at low temperatures, phonons are scattered only at the crystal surfaces. Heat transport under these conditions was first discussed by Casimir.[1] He considered a long, narrow sample with perfectly rough surfaces that scatter every incident phonon diffusely. The present study is concerned with crystals having highly specular (mirrorlike) surfaces, at which the phonons are scattered diffusely with only a small probability f. This specularity $(1-f)$ will increase the thermal conductance of the sample. We present our results for thermal conductance measurements on pure single crystals of polished silicon, and analyze these results in terms of phonon blackbody radiation. Our purpose is to understand the heat transport in these polished crystals, and to determine the diffuse scattering probability f from our thermal conductance measurements. In a previous study[2] the high sensitivity of diffuse phonon scattering to surface contamination was demonstrated qualitatively. Here we will show that thermal conductance measurements can be used as a precise *quantitative* tool for the study of surface defects and adsorbates in the temperature range of 0.05 to 1 K, which corresponds to a range of dominant phonon frequencies between ~ 5 and ~ 100 GHz. We obtain direct results for the diffuse scattering probability as a function of temperature, $f(T)$, for polished silicon crystal surfaces in this phonon frequency range. These phonon frequencies are not accessible using typical ultrasound, heat pulse, or superconducting tunnel junction techniques.[3] Other phonon generation and detection techniques also have limitations in frequency range and/or types of crystals which may be used.[4]

This investigation also serves a purpose of more general interest, namely the demonstration of the effects of sample geometry, and of black (emissivity$=1$) or grey (emissivity<1) objects, on the propagation of blackbody radiation. Although extensive work has already been done in the field of photon radiative transfer,[5] there are several advantages in performing theoretical and experimental studies of phonon radiation instead of photon radiation. Phonons in dielectric crystals will not convert into other excitations, while photons will "decay" into heat (phonons) when interacting with matter. Another advantage of phonon radiative heat transfer experiments is that the crystal provides a cavity which is bounded by an interface with a nonconducting medium, so that the phonons are completely contained within the crystal. Such experimental control is not possible with photon radiative heat transfer experiments. In the analysis of our experiments, the additional complexity of elastic anisotropy for phonon radiation is easily taken into account using Monte Carlo techniques, which will be discussed later.

The outline of the paper is as follows. Section II contains the experimental results, and shows that for highly polished samples the measured temperature difference ΔT between the two attached thermometers is fairly insensitive to the distance between them, but sensitive to the size of the thermometer clamps. Sections III, IV, and V each describe one of the three different analyses we have developed for phonon blackbody radiation. In Sec. III we present a simple one-dimensional (1D) model to describe qualitatively the effects of the attached thermometers. In Sec. IV, an integral expression for the heat flow through a cylinder with partially reflecting walls will be derived and solved by a Born-approximation method. The results of Sec. IV can be used to make an approximate determination of the diffuse scattering probability f in our experiments. In Sec. V, the algorithm for a Monte Carlo simulation will be presented, and the results of the simulation will be applied to the experimental data. The Monte Carlo techniques are necessary to obtain accurate quantitative information about both the specularity of polished surfaces, and the effect of thermometers on the radiative heat flow. The final result of this investigation is the diffuse scattering probability f as a function of temperature for our polished silicon crystals, as determined from the Monte Carlo simulations.

II. EXPERIMENTAL PROCEDURE AND PRELIMINARY RESULTS

The silicon crystals used for our thermal conductance measurements on polished samples were cut from *n*-type (phosphorous-doped) float-zone-refined silicon provided by SEH America. Their room-temperature resistivity was 780 Ω cm, and the dimensions of the crystals were 0.5 cm×0.5 cm×15 cm. The crystallographic orientation was ⟨111⟩ along the long axis of the crystal, and the side faces were ⟨110⟩ and ⟨211⟩. The final polishing step used Syton, a colloidal suspension of ~400-Å silica particles in a mild chemical etch. This is the standard procedure in the semiconductor industry. Before being mounted in the cryostat, the samples were ultrasonically cleaned in a 5:1:1 heated solution (85 °C) of distilled H_2O, 30% hydrogen peroxide, and ammonium hydroxide. This cleaning procedure was used to remove any organic contaminants, and was followed consistently for all samples to insure reproducible surfaces. The samples were then rinsed in distilled water, and remained in distilled water until being blown dry with nitrogen immediately prior to mounting. The effects of deviating from this polishing and cleaning procedure have been reported elsewhere.[2] The silicon crystals used for our measurements on rough samples were cut from a boule of *p*-type (boron doped) float-zone-refined silicon from Wacker Chemie. Their room temperature resistivity was 627 Ω cm, and the crystal size was 0.5 cm×0.5 cm×5 cm. The orientation of these crystals was the same as that of the 15-cm crystals. These crystals were also Syton polished, but their surfaces were subsequently roughened by sandblasting, and then cleaned with the procedure mentioned above, before being mounted in the cryostat.

The thermal conductance was measured using the two-thermometer and two-heater methods, described by Raychaudhuri.[6] The measurements below 1 K were carried out in a dilution refrigerator with a minimum operating temperature of about 50 mK; details of the experimental setup and technique are given elsewhere.[7] The thermal conductance above 1 K was measured in a pumped ^{4}He cryostat. The heater consisted of a 1000-Ω thin metal film evaporated onto a 1 mm×3 mm×0.25 mm sapphire substrate. Stycast 1266 epoxy was used to bond the sapphire chip to a flat polished piece of 0.020-in.-thick copper foil which was then soldered to the heater clamp. The copper foil was wrapped around the heater in an effort to capture any emitted radiation. Adequate thermal isolation between heater and cryostat was provided by three 1-in.-long 0.009-in.-diam constantan wires. Longer and thinner isolation leads became too resistive, and dissipated a significant fraction of their Joule heat by radiation. This radiated heat could be absorbed by the thermometers and affect their reported temperatures. Therefore, two pairs of thermometers (Allen Bradley resistors) were soldered to the copper clamps (described below), and both pairs were used to measure the temperature gradient of the sample, as a check that radiation problems had been made negligible. The equilibrium times for the heater and thermometers never exceeded a few seconds.

We refer to our experiments as thermal *conductance* measurements because they take place in a temperature range which is nearly devoid of the bulk phonon scattering required to give a uniform temperature gradient in the interior of the crystal, whereas thermal *conductivity* is by definition an intrinsic property of a material,[8] and should not depend on the size, shape, or surface conditions of the sample. Nevertheless, one can extract a temperature-dependent phonon mean free path $\bar{l}$ in the same manner as for thermal conductivity measurements, keeping in mind that this mean free path is not an intrinsic property of the silicon. Let us briefly review some basic definitions and formulae.

Thermal *conductivity* is determined by measuring the temperature gradient $\Delta T/\Delta x$ caused by a thermal power $\dot{Q}$ flowing uniformly through a rod-shaped crystal of cross section A:

$$\Lambda=\frac{\dot{Q}/A}{\Delta T/\Delta x} . \tag{2.1}$$

In the gas kinetic picture,[9] the thermal conductivity can be used to determine a phonon mean free path $\bar{l}$ within the dominant phonon approximation:

$$\Lambda=\tfrac{1}{3}C_v v\bar{l} , \tag{2.2}$$

where C_v is the Debye specific heat per unit volume. The average speed of sound v is given by

$$\frac{1}{v^3}=\tfrac{1}{3}\overline{\sum_{i=1}^{3}\frac{1}{v_i^3}} , \tag{2.3}$$

where the v_i are the group velocities of the three different modes, and the bar denotes an average over propagation directions. In the temperature range of our investigation, bulk scattering of phonons by lattice imperfections, impurities, and umklapp processes is negligible in the high-quality single crystals of silicon used in this work. In addition, bulk phonon-phonon scattering through N ("normal") processes is also negligible, so that phonon gas viscosity effects (such as Poiseuille flow[10]) are not present. Therefore, the phonons travel in straight ballistic paths, and can only be scattered at the crystal surfaces. In this boundary scattering regime, we can express the experimental quantity calculated with Eq. (2.1) (often loosely called a thermal conductivity) in a manner analogous to Eq. (2.2):

$$\Lambda=\tfrac{1}{3}C_v\bar{v}\bar{l} , \tag{2.4}$$

where $\bar{v}$ is an average speed of sound given by[11,12]

$$\bar{v}=\overline{\sum_{i=1}^{3}\frac{1}{v_i^2}}\Bigg/\overline{\sum_{i=1}^{3}\frac{1}{v_i^3}} . \tag{2.5}$$

If every phonon hitting the surface is diffusely scattered, e.g., in the case of rough sandblasted surfaces, then $\bar{l}$ is close to the sample diameter. Specifically, the Casimir limit is given by $\bar{l}_c=1.12\sqrt{A}$ for a long sample of square cross section A, and by $\bar{l}_c=2R$ for a long cylindrical sample of radius R.[1] If specular reflections can occur, the mean free path $\bar{l}$ will increase beyond this limit, i.e., the measured Λ will increase.

The surprising observations in this investigation were that the apparent thermal conductivities (and therefore the calculated $\bar{l}$) at low temperature depended not only on sample diameter and surface treatment, but also on the area of contact of the thermometer clamps, and the spacing between these clamps. In order to explore these effects, we used two different sets of thermometer clamps. One set had a contact area of $2\times(15\ \mathrm{mm}^2)$, and the other $2\times(1\ \mathrm{mm}^2)$. In order to optimize the mechanical contacts to the sample, the contact areas of the oxygen-free high-conductance (OFHC) copper clamps were coated with indium, which deforms as the clamps are fastened to the sample. The heater clamps also had a contact area of $2\times(15\ \mathrm{mm}^2)$, and the base clamps $2\times(25\ \mathrm{mm}^2)$. All the clamps were secured to the same two opposite faces of the sample. Figure 1 shows the four sample geometries used for measurements on polished samples. The measurements for rough samples were performed on the sandblasted 0.5 cm$\times$0.5 cm$\times$5.0 cm boron-doped crystals.

The effects of the different arrangements are shown in Fig. 2. The lowest curves (solid symbols) were obtained for the rough samples, and show no dependence on clamp size. For the polished samples (open symbols), clamp size and clamp spacing have a considerable influence on the measured "thermal conductivity." Not only is the apparent thermal conductivity of the polished samples much higher than the rough samples, as expected because of specular reflections, but the conductivities measured with the polished sample geometries shown in Figs. 1(a) and 1(d) differ by more than a factor of 4 at the lowest temperatures. These results demand an explanation.

In order to analyze these thermometer clamp effects, it is useful to determine an inverse phonon mean free path $\bar{l}^{-1}$ using Eq. (2.4), and this is shown in Fig. 3, along with data for the sample geometries shown in Figs. 1(b) and 1(c). Let us first consider our results for rough samples. The inverse phonon mean free path $\bar{l}^{-1}$ obtained for the rough samples is close to the Casimir limit of $(1.12\times0.50\ \mathrm{cm})^{-1}=1.79\ \mathrm{cm}^{-1}$, and is practically temperature independent. Our agreement with the Casimir limit will be discussed in more detail in Sec. V.

Now consider the data for the polished samples, specifically for the closely spaced large-clamp geometry

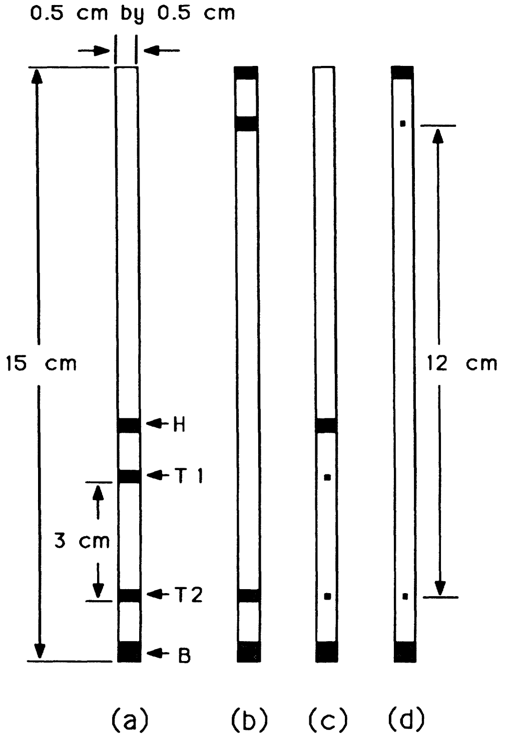

FIG. 1. The four different sample geometries used for thermal conductance measurements on polished samples. The heater, thermometer, and base clamps are denoted by H, T1, T2, and B, respectively. The contact surfaces of all the clamps were coated with indium. (a) Large thermometer clamps, close spacing. (b) The heater and warm thermometer clamps have been moved to the upper end of the sample. (c) Small thermometer clamps, close spacing. (d) Small thermometer clamps, distant spacing. The large thermometer clamps have an area of $2\times(15\ \mathrm{mm}^2)$, and the small thermometer clamps have an area of $2\times(1\ \mathrm{mm}^2)$.

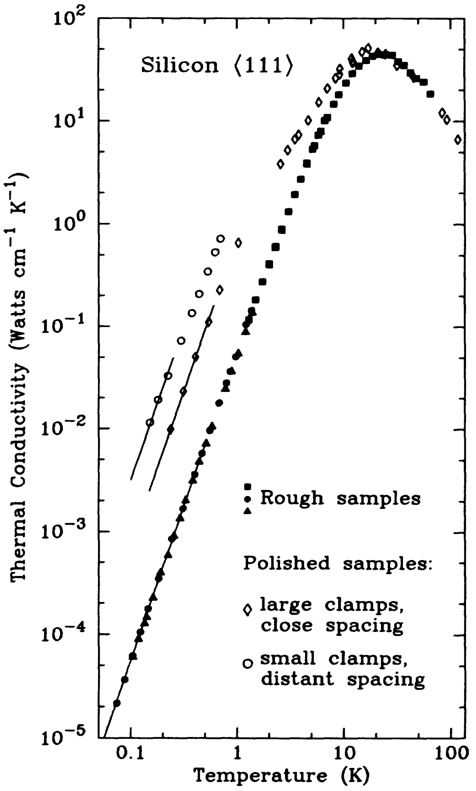

FIG. 2. The thermal conductivity of silicon (heat flow along ⟨111⟩) for samples with rough surfaces (solid symbols), and for polished samples (open symbols) with the geometries shown in Figs. 1(a) and 1(d). Note the surprising factor of >4 discrepancy between the thermal conductivities of the two polished samples below 1 K. These data illustrate that the measured thermal conductivity depends not only on the sample diameter and surface treatment, but also on the size and spacing of the attached thermometer clamps. The solid lines represent a fit to T^3.

of Fig. 1(a) [shown as curve (a) in Fig. 3], and the distantly spaced large-clamp geometry of Fig. 1(b) [shown as curve (b) in Fig. 3]. In these two cases, the calculated $\bar{l}^{-1}$ differ by about a factor of 4 at the lowest temperatures, which translates to a factor of 4 for the measured temperature gradients $\Delta T/\Delta x$ for a given $\dot{Q}$. The ratio of the two thermometer clamp separations Δx is also a factor of 4. Therefore it appears that the measured temperature *difference* ΔT (for a given $\dot{Q}$) is nearly independent of the separation of the thermometers. This observation indicates that the thermometers themselves are the dominant cause of the temperature difference they measure, and that any temperature difference due to diffuse phonon scattering at the crystal surfaces between the thermometers is small by comparison. Therefore we conclude that the surfaces of our polished silicon samples diffusely scatter only a small fraction of the incident phonons.

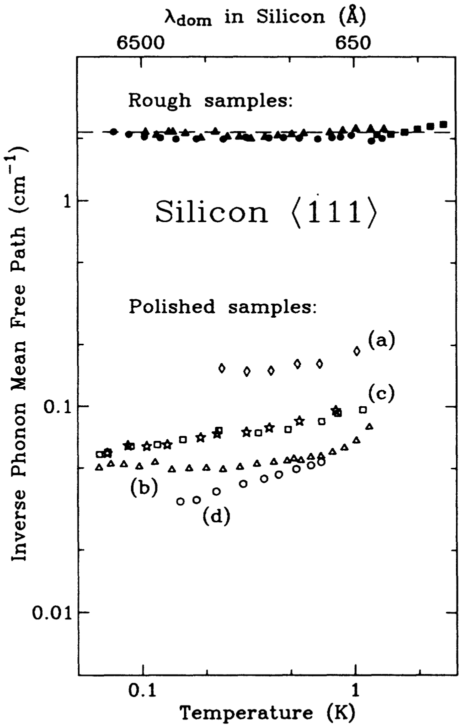

FIG. 3. The inverse phonon mean free path in silicon as a function of temperature for rough samples (solid symbols), and for the polished samples (open symbols) with the different clamping geometries shown in Fig. 1. (a) Open diamonds: large clamps, close spacing. (b) Open triangles: large clamps, distant spacing. (c) Open squares and open stars: small clamps, close spacing. (d) Open circles: small clamps, distant spacing. The $\bar{l}_{\rm expt}^{-1}$ shown here is the result of applying Eq. (2.4) to the data shown in Fig. 2. The experimental result for rough samples, $\bar{l}_{\rm expt}^{-1}=2.08$ cm^{-1}, is quite temperature independent, and agrees well with the result of the Monte Carlo simulation for that geometry: $\bar{l}_{\rm MCS}^{-1}=2.15$ cm^{-1} (shown as dashed line). For the two polished samples having the large clamp geometries shown in Figs. 1(a) and 1(b), the results show that the measured temperature difference between the thermometers is nearly independent of their spacing. The data shown in curve (c) are from two different experiments, and demonstrate the reproducibility of our results. All data were taken using the two-thermometer method, except for the solid-circle and open-diamond data, which were taken with the two-heater method. The equivalence of the two methods for an isotropic crystal is proven in Sec. IV.

This conclusion is further supported by the observation that for the experiments with the small thermometer clamps, the calculated $\bar{l}^{-1}$ was found to decrease even more [see curves (c) and (d) in Fig. 3]. We were careful to follow the same cleaning procedures for all our samples, and to then keep the crystal surfaces as free from contaminants as possible, before placing them under vacuum. The reproducibility of our experimental results is shown by the two different sets of data for the small clamps, close-spacing geometry [curve (c) in Fig. 3]. The same sample was used in both cases, but the heater clamp had been adjusted, and the sample had been exposed to air twice (for as long as a day) between the two data runs. We also found that recleaning our samples produced no change in the measured mean free path. Therefore we conclude that the clamp size and spacing effects are due to a real perturbation of the heat flow pattern in polished samples, and are not an experimental artifact. The purpose of the following section is to explain qualitatively the origin of these remarkable geometrical effects.

III. ONE-DIMENSIONAL MODEL

In this section, and in Sec. IV, we will present simplified models of our thermal conductance samples in order to (1) illustrate the principles of radiative heat transfer, (2) explain the physical origin of several surprising geometrical effects, including those discussed in Sec. II, and (3) provide a means of verifying the successful operation of the Monte Carlo calculation presented in Sec. V.

We begin our explanation with a simple, qualitative picture of photon blackbody radiation. Two parallel infinite black planar surfaces in vacuum, separated by the distance d, are held at the temperatures T_1 and T_2, respectively (see Fig. 4). In order to define a temperature between these planes, we consider an infinitesimal black thermometer in equilibrium with the photon radiation field at some point P. The thermometer receives radiation from both planes, and comes to an equilibrium temperature T_P when it reemits as much power as it absorbs. The solid angle subtended by either surface at point P is always 2π, so that the radiated power received will be independent of the position of P. Therefore, the temperature measured by the thermometer at P will be the same throughout the entire volume bounded by the surfaces, and is given by

$$T_P^4=\tfrac{1}{2}(T_1^4+T_2^4)\ . \tag{3.1}$$

Hence there must be discontinuous temperature jumps at the surfaces, as shown in Fig. 4(a). The temperature T_P is independent of the size of the thermometer. However, if a second thermometer is introduced, they will influence each other, unless both are infinitesimal. Figure 4(b) shows the temperature profile for the extreme case of an infinite black thermometer plane inserted between the two black surfaces at a position which contains the point P. The thermometer plane's temperature is also T_P as given by Eq. (3.1). A second *infinitesimal* thermometer will measure different temperatures, T_L or T_R, depending on whether it is located to the left or to the right of point P.

$$\begin{aligned} T_L^4 &= \tfrac{1}{2}(T_1^4 + T_P^4) , \\ T_R^4 &= \tfrac{1}{2}(T_P^4 + T_2^4) . \end{aligned} \tag{3.2}$$

Temperature jumps will now also occur on either side of the inserted thermometer plane.

Now consider two thermometers of finite size between the planes. They will tend to cast their shadows onto each other, which is to say that each thermometer will see a solid angle less than 2π from one of the planes. Instead, each will also receive radiation from the other thermometer, which is at some intermediate temperature. Therefore a temperature difference ΔT will be observed between the two thermometers, which will depend on the physical size of the two thermometers and also on their location. When the thermometers are small, they cast small shadows, and the temperature difference will be small. If we try to express ΔT in terms of an effective thermal conductivity of the radiation field, then smaller thermometers will report a large thermal conductivity. Infinitesimal thermometers would give $\Delta T = 0$, or an infinite thermal conductivity. Of course, the term thermal conductivity is a misnomer in this case.

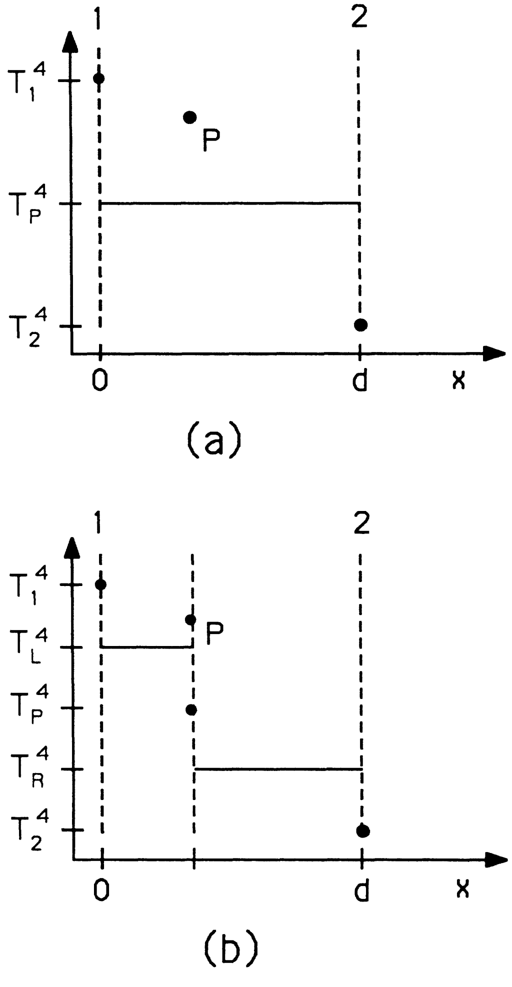

FIG. 4. (a) Two infinite planes (dashed lines), at temperatures T_1 and T_2, are positioned at $x=0$ and $x=d$. The point P lies somewhere in the volume bounded by the two planes. The temperature at the point P is independent of its location between the planes. At the planes discontinuous temperature jumps occur. (b) A third black plane is inserted between the other two so that it contains the point P. Now additional temperature jumps will occur on the inserted plane's left face as well as on its right face. The temperature measured by an infinitesimal thermometer now depends on whether it is located to the right (T_R) or to the left (T_L) of the inserted plane.

The results obtained for the two infinite planes remain unchanged if perfectly specular walls are inserted perpendicular to the planes, to represent a thermal conductivity sample with perfectly specular surfaces. The temperature profile along this sample is caused solely by the thermometers. If the walls are not perfectly specular, but partly diffusely scattering, then the temperature profile is determined in part by the thermometers, and in part by the walls. We will see in the following discussion that the experimental results shown in Figs. 2 and 3 can be understood within this basic qualitative picture.

In order to provide an exactly soluble model of phonon radiative heat transfer which includes the effects of the attached thermometers and the diffuse phonon scattering at the free surfaces of the sample, we will consider a simplified representation of the geometry of the samples used in our experiments. We replace the rectangular rod-shaped sample with a specular cylindrical sample, and represent the diffusely scattering surface of the sample by a series of thermalizing surfaces (or sheets) perpendicular to the axis of the specular cylinder. We call this representation of our samples the "model of sheets." Figure 5(a) shows a cylindrical solid of diameter D, dimensionless length-to-diameter ratio L, cross sectional area $A = \pi D^2/4$, and with perfectly specular surfaces. Although our model uses a cylinder of circular cross section, the results are unchanged for rectangular cross sections having the same area A. The N sheets which represent the surface of the sample are labeled 1 to N, while we represent the ends of the sample by the sheets labeled 0 and $N+1$. The ith sheet is given an emissivity which is related to the diffuse scattering probability f of the surfaces of the sample in the experiments, and so for notational convenience we refer to this emissivity as f_i. The ith sheet, at temperature T_i, then captures a fraction f_i of all phonon radiation incident on it, and reemits a power $f_i \sigma T_i^4$ in each direction. Since the sheets are thermalizing, the phonon radiation absorbed by each sheet is reemitted with a $\cos\theta$ angular distribution, in accord with Lambert's Law for blackbody radiation, where θ is the angle with respect to the normal of the surface of a sheet. Since each sheet is reflected out to infinity by the walls of the specular cylinder, we have in effect a one-dimensional model of heat transport similar to the 1D model of the infinite thermalizing planes discussed earlier in this section. Specifically, the heat flux along our cylinder of sheets is uniform over its cross section, since we are ignoring elastic anisotropy in this model. Therefore the angle of emission, θ, is irrelevant, and we need consider

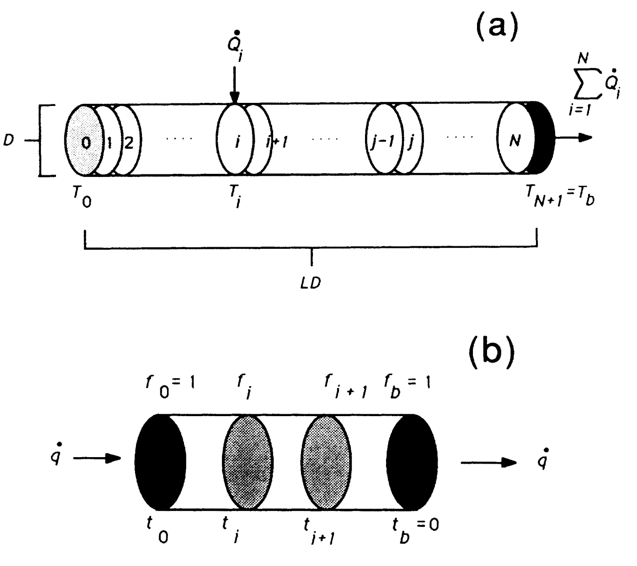

FIG. 5. (a) A one-dimensional model for radiative heat transfer. Each element of the sample surface, including the clamped area, is represented by a thermalizing sheet perpendicular to an otherwise specular tube of cross-sectional area A, which absorbs a fraction f_i of the radiation passing through it. All the heat leaves through the rightmost element, which represents the point at which the sample is clamped to the cryostat. (b) Reduced model of 1D heat transfer, for calculating the temperature drop between elements i and $i+1$ of the model shown in (a). By iteration, the entire solution may be obtained.

only the side of the sheet from which the phonon is emitted. We constrain the ends of the cylinder by specifying that the 0th sheet does not radiate to the left, and that the $(N+1)$th sheet does not radiate to the right. If we take both ends to be black ($f_0=f_{N+1}=1$), then we need not keep track of multiple reflections from the ends of the cylinder, and the discussion of heat transfer takes on a particularly simple form. We can define our phonon Stefan-Boltzmann constant σ in analogy to that used for photon radiation

$$\sigma \equiv \frac{\pi^2 k^4}{40\hbar^3} \overline{\frac{1}{3} \sum_{i=1}^{3} \frac{1}{v_i^2}} , \tag{3.3}$$

where the v_i are the group velocities of the three different phonon modes, and the bar denotes an average over propagation directions (for the case of an elastically anisotropic crystal). For silicon, σ is about 18 mW/cm^2 K^4.

Let $\dot{Q}_i$ be the external thermal power supplied to the ith sheet (for $\dot{Q}_i > 0$) or the heat extracted from the ith sheet (for $\dot{Q}_i < 0$). Let a'_{ij} equal the product of the probability of emission from sheet j and absorption in sheet i without absorption by any of the sheets between i and j, or

$$a'_{ij} = f_i f_j (1-f_{j-1}) \cdots (1-f_{i+1}) \quad \text{for } j > i \tag{3.4}$$

and $a'_{ij} = a'_{ji}$. The system of sheets is in equilibrium when the sum of the radiant energy received from all the other sheets and the power supplied from the environment is equal to the power radiated by each sheet. That is,

$$A\sigma \sum_{j\,(\neq i)} a'_{ij} T_j^4 + \dot{Q}_i = \delta_i \sigma f_i A T_i^4 \tag{3.5}$$

for $i=0$ to N, where $\delta_i = 2$ for $1 \le i \le N$ and $\delta_i = 1$ for $i=0$ and $N+1$. This system of equations has solutions with all $T_i^4 > 0$ only when $\sum_{i=0}^{N+1} \dot{Q}_i = 0$. Hence we may eliminate one of these $N+2$ equations with this constraint, and it is most natural to do so by identifying the $(N+1)$th sheet with the base of the sample at some fixed temperature T_b, through which all the heat inputs leave the sample. Then $T_b \equiv T_{N+1}$, $f_b \equiv f_{N+1}$, and $\dot{Q}_{N+1} = -\sum_{i=0}^{N} \dot{Q}_i$, and we eliminate the base from further consideration. We may rewrite the remaining N equations in matrix form as

$$A\sigma \underline{a} (\mathbf{T}^4 - T_b^4) = \dot{\mathbf{Q}} , \tag{3.6}$$

where $a_{ij} = -a'_{ij}$ $(i \neq j)$, $a_{ii} = 2f_i$ $(i \neq 0)$, and $a_{00} = 1$. We have used the identity $\sum_{j=0}^{N+1} a_{ij} = 0$ for each i, which expresses the fact that a phonon emitted from one surface must eventually be absorbed somewhere else. The elements of $\mathbf{T}^4$ are the T_i^4 and the elements of $\dot{\mathbf{Q}}$ are the $\dot{Q}_i$.

If the temperature drop along the sample is small compared to T_b, it is convenient to convert Eq. (3.5) from linear in T^4 to linear in T. We define a reduced temperature $t_i = (T_i - T_b)/T_b$ so that $T_i^4 = T_b^4(1+t_i)^4 \approx T_b^4 + 4T_b^4 t_i$ for $t_i \ll 1$. We rearrange to obtain

$$\mathbf{t} = \underline{a}^{-1} \dot{\mathbf{q}} ,$$

where $\dot{\mathbf{q}}_i = \dot{Q}_i / 4\sigma T_b^4 A$, and $\underline{a}$ is the same as before. The reduced temperature at the base, t_b, is now equal to zero. When only $\dot{q} \equiv \dot{q}_0$ is nonzero, the problem is easily solved. Consider sheets i and $i+1$ in isolation. Because of the 1D nature of the problem, the net $\dot{q}$ must be same between any two sheets. We do not know the average temperature of these two elements, since the addition of a uniform temperature to all elements results in no net heat flux. However, the net radiative exchange between i and $i+1$, and hence the temperature difference $t_i - t_{i+1}$, is identical to that of the greatly simplified and easily solved model of Fig. 5(b), for which $f_0 = f_b = 1$, $f_1 = f_i$, and $f_2 = f_{i+1}$. We eliminate the rightmost sheet as before and obtain

$$\underline{a} = \begin{bmatrix} 1 & -f_i & -f_{i+1}(1-f_i) \\ -f_i & 2f_i & -f_i f_{i+1} \\ -f_{i+1}(1-f_i) & -f_i f_{i+1} & 2f_{i+1} \end{bmatrix} . \tag{3.7}$$

In this case $\underline{a}$ may be easily inverted, and we find

$$t_i - t_{i+1} = \dot{q}(a_{10}^{-1} - a_{20}^{-1}) = \dot{q} \left[\frac{f_i + f_{i+1} - f_i f_{i+1}}{(2-f_i)(2-f_{i+1})} \right] . \tag{3.8}$$

This result applies for all i. We iterate to get the solution for any N and any set of f_i.

To simulate a sample of uniform f, we let $N \to \infty$ and set $F_i = fL/N$ for $i \neq 0$, $N+1$. Applying Eq. (3.8), we find a temperature drop of $\dot{q} fL/2N$ between adjacent sheets for $i \neq 0, N$, which for N/LD sheets per unit length gives a uniform temperature gradient of $\dot{q}f/2D$. At the ends, however, $t_0 - t_1 = t_N = \dot{q}/2$, since $f_0 = 1$ and $f_1 \to 0$, $f_N \to 0$ with $f_{N+1} = f_b = 1$. Since the sheets are spaced arbitrarily closely in the limit, we have discontinuous jumps of $\dot{q}/2$ at each end with a linear profile in between, as suggested by the discussion earlier in this section concerning infinite planes.

For clean polished samples, the area under the thermometer clamps will scatter radiation much more effectively than an equal area of the exposed surface. Figure 6 shows a typical sample with thermometers at H and C and a heater at the top, and having walls of diffuse scattering probability f. The clamp-free part of the sample is represented as just described, while the clamps are represented by individual sheets with $i = h, c$ and with $f_h = f_c = \alpha$, where α is the probability that a clamp scatters radiation as it passes through the sample. Again applying (3.8) with $i = h-1, h, c-1, c$ and noting that

$$f_{h-1} = f_{h+1} = f_{c-1} = f_{c+1} = f/N \to 0 \ ,$$

we find a jump of $\dot{q}\alpha/2(2-\alpha)$ between elements $h-1$ and h as well as between h and $h+1$, with the same result for c. Thus the measured temperature difference $T_h - T_c$ includes a contribution

$$\frac{\dot{Q}\alpha}{4\sigma T_b^3 A (2-\alpha)}$$

from the clamps themselves, which in the model of sheets is independent of their separation.

The temperature profile of the sample with $f \neq 0$ and with thermometers attached is shown in Fig. 7. The profile is linear with gradient $\dot{q}f/2D$ derived above, and has discrete jumps at the ends independent of sample length or the presence of clamps, as well as jumps at the clamps proportional to their area as a fraction of the total cross section of the sample. Previous investigators[13,14] have assumed a linear profile along the entire sample, neglecting the jumps at the ends and at the clamps. For finite samples of high specularity this leads to serious errors in converting a measurement $(T_h - T_c)$ into the quantity of interest (f) as $f \to 0$. Neglecting the temperature jumps at the ends gives a calculated f which is too low; neglecting the temperature jumps at the clamps gives a calculated f which is too high.

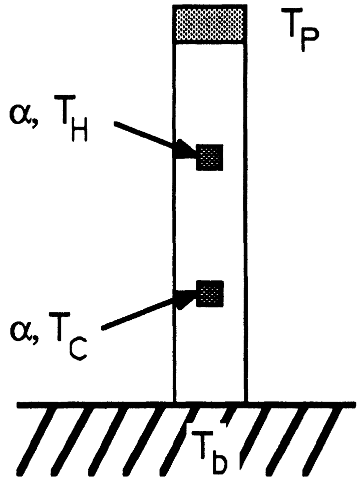

FIG. 6. Typical locations of heaters, thermometer clamps, and the base heat sink on a sample. The two-heater method of measuring thermal conductance puts in heat at H or C and measures T_P. The two-thermometer method puts in heat at P and measures T_H and T_C. The shaded squares at H and C represent the area under a clamp, which scatters phonons much more strongly than the clean surface. A fraction α of the phonons passing down the sample are scattered diffusely at the clamps.

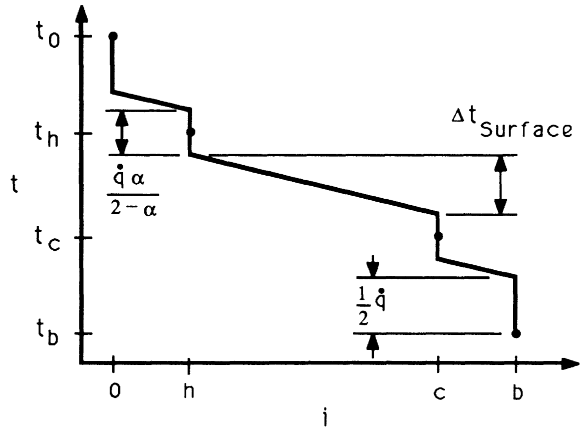

FIG. 7. Linearized temperature profile in the model of sheets representation of a sample with a nonzero diffuse scattering probability f at the surface, and with clamps which scatter a fraction $\alpha = \frac{1}{3}$ of the phonons passing by them.

IV. GENERAL ANALYSIS AND CYLINDRICAL SOLUTION

This section presents the mathematical basis for two interesting results: the equivalence of the two-heater and two-thermometer methods of measuring thermal conductance in the radiative regime, and the temperature profile and thermal conductance of a cylinder with highly specular walls.

The general analysis of radiative heat transfer in an enclosure, which in our case is the surface of the sample, is computationally difficult, though the physical and mathematical principles are described in the engineering literature.[5] A conceptually useful and simple way of discussing the problem is to divide the surface into a finite number of discrete elements and proceed as in Sec. III. To eliminate unnecessary complication we suppose that the sample is elastically isotropic and that the diffuse scattering probability f of the sample's surface is independent of the phonon's angle of incidence.

The surface S of the sample is divided into small planar elements i of area S_i at temperature T_i, with diffuse scattering probability f_i, and with unit normal $\hat{n}_i$. The points in S_i are labeled $\mathbf{r}_i$. The direct view factor F_{ij} is defined as the fraction of the radiative energy leaving element j which strikes element i without striking any other surfaces an route. We assume that the scattered radiation leaves element j with a cosine distribution according to Lambert's law. This assumption makes f_i equivalent to an emissivity in this model.[15] From Fig. 8, we can see that

$$F_{ij}=\frac{1}{S_j}\int\int\frac{\cos\theta_i\cos\theta_j}{\pi r_{ij}^2}dS_i\,dS_j \tag{4.1}$$

where $\mathbf{r}_{ij}=\mathbf{r}_i-\mathbf{r}_j$, and the surface integral is over all $\mathbf{r}_i$ in i and all $\mathbf{r}_j$ in j.

The total view factor in the presence of specular reflection, F_{ij}^s, is the fraction of the radiative energy leaving j which strikes i directly or after specular reflections (but not after being diffusely scattered). It is the sum of direct view factors

$$F_{ij}^s=F_{ij}+\sum_{k=1}^{\infty}\sum_{S}(1-f_m)(1-f_n)\cdots(1-f_p)\times F_{ij(m,n,\ldots,p)}\ , \tag{4.2}$$

where $F_{ij(m,n,\ldots,p)}$ is defined as the direct view factor from the reflected image of element j to element i after reflection of element j through the planes of elements $m,n,\ldots,p$, while $F_{i(m,n,\ldots,p)j}$ is defined as the direct view factor from element j to the reflected image of element i. The k surface elements $m,n,\ldots,p$ are selected to account for all possible paths giving k specular reflections between elements j and i, with $\sum_S$ denoting the sum over all such sets of k surface elements.

Since the power transferred from element j to element i is the area (S_j) times the radiant flux per unit area from j ($\sigma f_j T_j^4$) times the fraction leaving j which strikes i (F_{ij}^s) times the fraction intercepted by i (f_i), we can express radiative equilibrium among the surface elements of a specular sample as

$$\sigma\sum_j S_j f_i f_j F_{ij}^s T_j^4+\dot{Q}_i=\sigma S_i f_i T_i^4\ . \tag{4.3}$$

Note that, unlike Eq. (3.5), the $i=j$ term is not excluded, which means that, in a specular 3D sample, photons can leave a surface element, be reflected specularly several times, and return to the element from which they started. Comparison of Eq. (3.5) with Eq. (4.3) suggests that we define $a_{ij}'=-a_{ij}=f_i f_j S_j F_{ij}^s$ $(i\neq j)$, $a_{ii}=f_i S_i(1-f_i F_{ii}^s)$, and divide by S_i rather than A to obtain the reduced power inputs $\dot{q}_i$. Then we can apply the matrix equations of Sec. III, with the additional notation that $T_k(l)$ denotes the temperature of the kth element when heat is put only into the lth element and removed from the base of the sample.

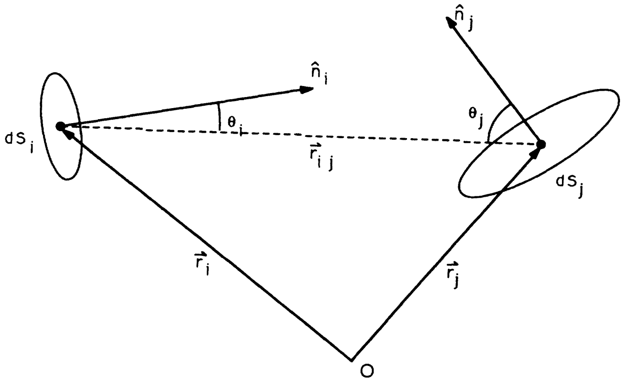

FIG. 8. Two infinitesimal surface elements of an enclosure in direct line of sight.

Let $\underline{m}$ denote the operation of reflection through the plane of element m. Choose a coordinate system so that element m is in the xy plane. Then it is straightforward to show that $\hat{\mathbf{n}}_i\cdot(\mathbf{r}_i-\underline{m}\mathbf{r}_j)=\underline{m}\hat{\mathbf{n}}_i\cdot(\underline{m}\mathbf{r}_i-\mathbf{r}_j)$ and that $|(\underline{m}\mathbf{r}_i-\mathbf{r}_j)|=|(\mathbf{r}_i-\underline{m}\mathbf{r}_j)|$. Then $S_jF_{ij(m)}=S_jF_{i(m)j}=S_iF_{ji(m)}$. By extending this reasoning to an indefinite number of reflections we can show $S_jF_{ij(m,n,\ldots,p)}=S_iF_{ji(m,n,\ldots,p)}$ and $\underline{a}$ is symmetric as before.

Using the formalism just developed, we can now show the equivalence of the two-heater and two-thermometer methods for measuring the thermal conductance of an isotropic sample. The two-heater method measures the temperature difference at a thermometer at point P, represented by element p, when $\dot{Q}$ is put into the sample at H (element h) or C (element c). The two-thermometer method measures the temperature difference between H and C when $\dot{Q}$ is put in at P. Typically, P is at the end of the sample furthest from the thermal ground, while H and C span most of the sample's length, as shown in Fig. 6. From the solution of the matrix equation, $t_h(p)-t_c(p)=q(a_{hp}^{-1}-a_{cp}^{-1})$, while $t_p(h)-t_p(c)=q(a_{ph}^{-1}-a_{pc}^{-1})$. Since $\underline{a}$ is symmetric, so is its inverse, and both methods give the same temperature difference for the same power input (see the caption for Fig. 3).

Although one could use Eq. (4.3) to solve the problem of radiative transfer for an arbitrary sample, the large number of planar surface elements required to model an arbitrary surface requires one to invert prohibitively large matrices, and in the presence of many specular reflections the determination of the F_{ij}^s becomes cumbersome. Much better insight into the problem is gained by considering samples of high symmetry and using surface elements invariant under this symmetry, such as the problem of a cylinder with diffusively scattering walls. In this case the elements are taken to be the black disks at the ends of the cylinder, of diameter D and length LD, and bands of width Ddx a distance Dx from the hot end (see Fig. 9). The diffuse scattering probability of the walls is f, and $f=1$ at the ends. The temperature at x is $T(x)$, with $T_b\equiv T(L)$.

One then writes Eq. (4.3) using these elements and view factors and goes to the limit of infinitesimal bands and an integral rather than a sum. Using the following definition for a normalized temperature profile,

$$\Phi(x)\equiv\frac{T^4(x)-T_b^4}{T^4(0)-T_b^4}\approx\frac{4T_b^3(T(x)-T_b)}{4T_b^3(T(0)-T_b)}=\frac{t(x)}{t(0)}\quad [t(x)<t(0)\ll 1]\ , \tag{4.4}$$

Perlmutter and Siegel[15] derive an integral equation for the temperature profile of the cylinder:

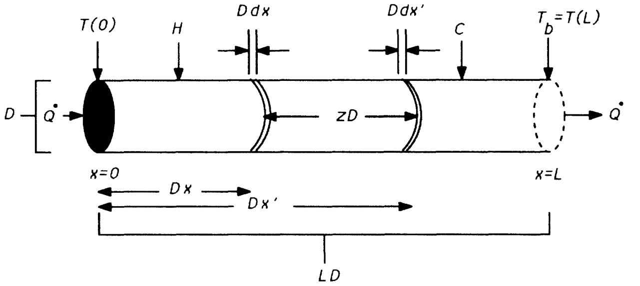

FIG. 9. Elements of the surface for the three-dimensional treatment of the problem of radiative heat transfer in a cylinder with uniform diffuse scattering probability f at the surface. Lengths (x,z,L) are in units of the diameter D. Points H and C are typical locations for heaters or thermometers. Power $\dot Q$ is incident from the left.

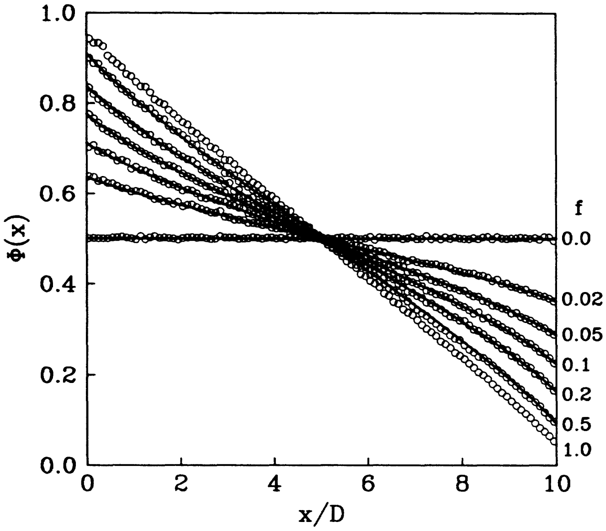

FIG. 10. Normalized temperature profiles for an open ended cylinder which is heated by radiation at the left by a cross sectional sheet of uniform temperature. The profiles have been calculated for different diffuse scattering probabilities f of the radiation quanta at the surface of the cylinder. The solid lines are the result of solving the radiative heat transfer equations using a Born approximation, as described in Sec. IV. The circles are the result of a Monte Carlo simulation discussed in Sec. V. The ordinate $\Phi(x)$ is equal to the quantity $T^4_{\mathrm{norm}}(x)$ used in Sec. V. The diameter of the cylinder is D, and the length to diameter ratio is $L=10$.

$$\Phi(x)=F_f(x)+f\int_0^L \Phi(x)G_f(\,|x-x'|\,)dx' \ , \qquad (4.5)$$

where $F_f(x)$ is the total view factor between the hot end and the band at x when the diffuse scattering probability is f, and $G_f(z)$ is the total view factor between two bands a distance $z=|x-x'|$ apart. F_f and G_f are sums of a series of elementary functions which converge to 1% of their final values in at most $4/f$ terms. Once they have been generated for a given f they can be used without recomputation for all L. For the case of a cylinder with completely specular walls ($f=0$), it can be shown that $F_0=\frac{1}{2}$ and $\lim_{f\to 0} fG_f=0$, and therefore the temperature profile is given by $\Phi(x)=\frac{1}{2}$, which corresponds to the constant temperature between the sheets in Fig. 4(a).

There are several techniques for numerically solving Eq. (4.5) in an efficient way. The most rapid procedure for long tubes and small f, given the functions F_f and G_f, is to iterate, a procedure familiar from scattering theory as the Born approximation (BA):

$$\Phi(x)_{n+1}=F_f(x)+f\int_0^L \Phi_n(x)G_f(\,|x-x'|\,)dx' \qquad (4.6)$$

where $\Phi_0(x)=\frac{1}{2}$. The series converges for $fL<5$, which for typical sample dimensions ($L\approx 10$) limits this technique to $f<0.5$.

This technique can easily give a high-resolution profile of 200 points along the axis of the cylinder. The results for $L=10$ are the solid lines in Fig. 10. The results of a Monte Carlo calculation (described in Sec. V) are shown as the circles in the figure; the two methods give indistinguishable results. At low f there is a pronounced curvature in the profile near the ends, as well as the jumps at the ends suggested by the 1D model. Given $\Phi(x)$ from this solution, we can calculate the net heat flux along the axis of the tube, which is the difference between the heat radiated in by the left end and the heat radiated back out the left end by the wall:

$$\dot q = t(0)\left[1-4f\int_0^L \Phi(x)F_f(x)dx\right] \qquad (4.7)$$

where $\dot q=\dot Q/\pi\sigma D^2 T_b^4$. The kinetic relation $\Lambda=\frac{1}{3}C_v\bar v l$ [Eq. (2.4)] and the equation $\Lambda\, dT/dx=\dot Q/A$ [cf. Eq. (2.1)] allow us to use the nearly linear central regions of these profiles to define a mean free path for phonons in this calculation:

$$l_{\mathrm{cyl}}^{-1}(f,L)=\frac{4t(0)}{3D\dot q}\frac{d\Phi}{dx}\bigg|_{x=L/2} \ , \qquad (4.8)$$

where $l_{\mathrm{cyl}}^{-1}(f,L)$ denotes the inverse scattering length for phonons in a cylinder with walls of diffuse scattering probability f and of dimensionless length to diameter ratio L.

With the results of this section and Sec. III, we have a crude procedure for including clamp effects and a realistic temperature profile to obtain f from T_H-T_C. First, estimate the contribution due to the clamps alone, $\Delta T_{\mathrm{clamps}}$, either by measuring T_H-T_C as the clamp spacing Δx (here not dimensionless) goes to 0, or by estimating α, which will be roughly equal to one-half the ratio of the clamp area to the total cross section, and applying the result of the model of sheets. Then calculate the temperature drop between H and C due to surface scattering alone, $\Delta T_{\mathrm{surf}}\equiv T_H-T_C-\Delta T_{\mathrm{clamps}}$, and use this to calculate the inverse phonon mean path for the experiment:

$$l_{\mathrm{expt}}^{-1}\equiv\frac{1}{3}C_v\bar v\frac{\Delta T_{\mathrm{surf}}}{\Delta x}A/\dot Q=\frac{4\pi\sigma D T_b^3\Delta T_{\mathrm{surf}}}{3\dot Q\Delta x} \ , \qquad (4.9)$$

where $A=\pi D^2/4$ and $16T^3\sigma=C_v\bar v$. We can then prepare curves of $l_{\mathrm{cyl}}^{-1}(f,L)$ versus f for various L (as shown in Fig. 11), and when the thermometers or heaters

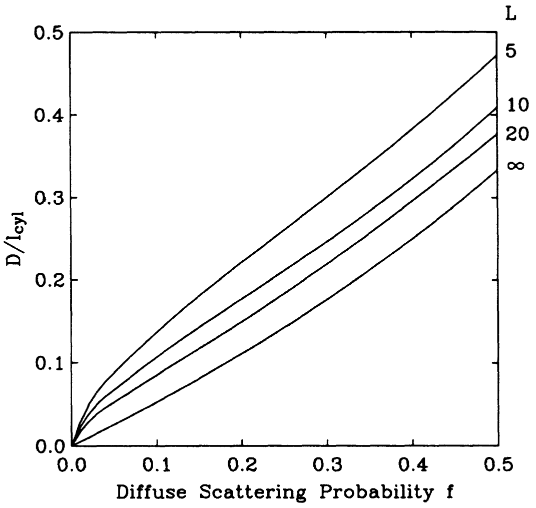

FIG. 11. Inverse mean free path l_{cyl}^{-1} for phonons in a cylinder with diameter D, length to diameter ratio L, and diffuse scattering probability f at its surface. The cylinder used is the same as that of Fig. 9.

of the experiment are located in the nearly linear part of $\Phi(x)$, we can compare l_{expt}^{-1} with $l_{\text{cyl}}^{-1}(f,L)$, and then interpolate for the appropriate L to find f.[16]

For more accurate results, we must use the exact sample dimensions, clamp sizes, and clamp spacings, and include the elastic anisotropy of the crystal. There is no tractable analytic technique that includes these departures from the ideal case studied above, and we must instead perform a Monte Carlo calculation, which will be discussed in the following section.

V. MONTE CARLO SIMULATIONS AND DATA ANALYSIS

A. Introduction

As described in the preceding section, the radiative heat transfer equations can be solved exactly for three-dimensional heat flow in simple geometries with simple boundary conditions at the surfaces. These solutions yield temperature profiles and heat fluxes which can be used to determine an effective mean free path for the heat quanta, but the simple geometries are difficult or impossible to produce in an actual thermal conductance experiment. Hence any comparison between calculated and experimental mean free paths is only approximate.

This section describes the algorithm and application of a Monte Carlo simulation that models the phonon heat transport in a crystal of arbitrary shape, size, and surface conditions. The simulation produces a temperature profile along the direction of heat flow in the crystal, showing quantitatively the effects of attached thermometer clamps on the measured temperature gradient $\Delta T/\Delta x$. From the total heat conducted through the sample in the simulation, a phonon mean free path $\bar{l}_{\text{MCS}}$ can be extracted. This mean free path is a function of the diffuse scattering probability f chosen for the free surfaces of the crystal in the simulation. Therefore, a quantitative comparison of $\bar{l}_{\text{MCS}}(f)$ with $\bar{l}_{\text{expt}}$, obtained in an actual experiment for the sample sample geometry, yields the effective diffuse scattering probability f in the experiment.

B. Prerequisite definitions and assumptions

Before describing the algorithm of the Monte Carlo simulations, we will first discuss some definitions and assumptions present in the analysis. The temperature at the crystal surface in the simulation is defined in the same way that it was defined in the beginning of Sec. III: as the temperature that would be measured by an infinitesimal thermometer at the surface and in equilibrium with the phonon radiation field. The Stefan-Boltzmann law is given by

$$P_e = \epsilon \sigma T^4 . \tag{5.1}$$

Here P_e is the phonon power per unit area which is absorbed and reemitted from the infinitesimal thermometer, T the temperature of the thermometer, ϵ the emissivity of the thermometer, and σ is the phonon equivalent of the Stefan-Boltzmann constant as given by Eq. (3.3). For simplicity, let us chose $\epsilon=1$ for our infinitesimal thermometer. The thermometer does not significantly perturb the radiation field, and hence it will receive the same radiation flux that the bare crystal surface would receive. In addition, the power per unit area *leaving* the crystal surface is the same as that leaving the thermometer, since energy is conserved in both cases. All the phonons leaving the thermometer have been absorbed and reemitted ($\epsilon=1$), whereas those leaving the bare crystal surface have only been diffusely scattered or specularly reflected. Nevertheless, the two total powers per unit area are the same. Therefore the temperature at a given point on the crystal surface is given directly by Eq. (5.1) with $\epsilon=1$, and where P_e is now the *total* phonon power per unit area leaving the crystal surface, *regardless of whether these phonons were absorbed and reemitted, diffusely scattered, or specularly reflected.*

At this point we should also make an important distinction between the emissivity of a crystal surface ϵ and the diffuse scattering probability f. The difference lies in the momentum and energy distributions of the emitted phonons. The emissivity gives the probability for a phonon to be absorbed by the surface (i.e., by some body in contact with the crystal, such as a thermometer clamp), which is the same as the probability for phonons to be emitted from the surface with the cosine distribution for blackbody radiation as given by Lambert's law:

$$P_e(\theta)d\Omega \propto \cos(\theta)d\Omega . \tag{5.2}$$

Furthermore, the *energy* distribution of these emitted phonons is the Planck distribution, with the dominant phonon energy proportional to the temperature. These phonons have thermalized; the phonon absorbed is not the same phonon that is reemitted. It can be shown[17] that the angular and energy distributions of these reemitted phonons is always given as described above, whether or not the surface is in thermal equilibrium with its surroundings.

No such general distribution holds for phonons which are merely diffusely scattered by a rough surface; in this case the incident phonons are not absorbed and thermalized, but are scattered back from the surface with an angular distribution that depends on the microscopic nature of the surface roughness. For instance, the surface may be locally smooth on the length scale of the phonon wavelength, but jagged on a larger length scale. In this case, the phonon will reflect specularly from small oblique surfaces, giving an average emission distribution that is a function of the surface geometry. It is also possible that some of the phonon scattering does not come from surface roughness, but from point defects and grain boundaries just below the surface, which were created by the polishing procedure (or by the sandblasting procedure in the case of roughened samples). Another mechanism could be phonon absorption and reemission from excited states of molecular adsorbates, giving an emission distribution which would depend on the adsorbed species. In spite of all of these considerations, in our Monte Carlo simulations and in the analysis of Sec. IV, we have made the arbitrary but simplifying assumption that diffusely scattered phonons leave a surface with a cosine distribution as in the case of a black ($\epsilon=1$) surface. We believe that this assumption is reasonable because the simulations for our rough $\langle 111 \rangle$ samples give a phonon mean free path which compares very well with that obtained in our experiments. Furthermore, we have experimented with other emission distributions in our simulations, and have found that the resulting phonon mean free paths are rather sensitive to the chosen distribution. We also believe our assumption is reasonable because a cosine distribution has been observed experimentally for diffuse scattering of light by a rough surface.[18]

If a phonon is not absorbed and reemitted or diffusely scattered, then we assume that it is perfectly specularly reflected. In other words, the total angular distribution of emission is the sum of only two distributions: a specular distribution and a cosine distribution. There is one parameter in the simulations which needs to be determined experimentally before the simulations can be used to determine the diffuse scattering probability f at the free surfaces of the crystal. This parameter is the effective emissivity of the indium coated copper clamps which are in contact with the silicon surface, expressed as ϵ_{clamps}. Our procedure for determining ϵ_{clamps} is described in Appendix B.

In the Monte Carlo simulations we also give all phonons the same energy, so that the diffuse scattering probability f is the same for all phonons in the crystal. When we compare our results for $\bar{l}_{\text{MCS}}(f)$ to $\bar{l}_{\text{expt}}$ at a given temperature, we are then making a dominant phonon approximation. Within our monochromatic assumption used in the simulations, a thermalizing surface ($\epsilon>0$) will manifest a greater temperature by merely emitting *more* phonons, and not phonons of a higher energy. These two types of emission are statistically equivalent in the Monte Carlo simulations; all that is required is that the thermalizing surface satisfies the Stefan-Boltzmann equation for the total thermal power emitted, and that the emission has a cosine angular distribution.[15] A diffusely scattering surface ($f>0$) does not generally change the energy of the scattered phonon,[19] and therefore this process does not require any simplification in the Monte Carlo simulations, except to have a purely cosine emission distribution.

C. Algorithm and analysis used for the simulations

With the above assumptions and definitions taken into consideration, we now begin the discussion of the algorithm used in the Monte Carlo simulations. The simulations model the crystal as an enclosure with walls that are treated as either specularly reflecting, diffusely scattering, or absorbing and reemitting surfaces for the phonons. The phonons are treated as indivisible point particles. A simulation begins by emitting one phonon from a random location on the surface in contact with the heater clamp, and with a random momentum vector given by a cosine angular distribution. The next intersection point of the phonon with the crystal surface is then calculated. If the diffuse scattering probability at that point is f, then the phonon has a probability f of being reemitted from the same point with a cosine distribution, otherwise it will be reflected specularly. As in Sec. IV, we assume for the simulations that the diffuse scattering probability f is independent of the phonon's angle of incidence. The unpolished 0.5 cm$\times$0.5 cm end surfaces of the crystal are given a diffuse scattering probability of $f=1$. When the phonon strikes a point in contact with a thermometer having emissivity ϵ_{clamps}, it has a probability ϵ_{clamps} of being absorbed by the thermometer, whereupon it is immediately reemitted with a cosine distribution from a *random* location on the thermometer clamps's contact area. The point of emission is random since the reemitted phonon is not necessarily the same phonon that was absorbed by the thermometer. These reemitted phonons, as well as diffusely scattered phonons, are also emitted with a random polarization mode (either the longitudinal mode or one of the two transverse modes). The choice of polarization is weighted by the relative densities of states of the three modes. The path of a phonon is followed until it either (1) strikes the area in contact with the base clamp, whereupon it is permanently absorbed, or (2) strikes the area in contact with the heater, *where it is also permanently absorbed.* At this point a second phonon is emitted from the heater, and the process is repeated.

The reader may wonder what role time or the velocity of the phonon plays in this simulation. The answer is none. Ideally, the phonons should be emitted as a certain number per unit area *per unit time* from the heater, in order to define a temperature at the heater. However, since phonons do not interact with each other in the boundary scattering regime, they can be emitted at any time during the simulation, and only the total number of emitted phonons needs to be recorded. The average power emitted by the heater is then determined by the arbitrary amount of time for the simulation to take place: t_{MCS}. All phonons in the simulation have the same arbitrary energy E_{ph}, and therefore make identical contributions of

$E_{\rm ph}/t_{\rm MCS}$ to the total power emitted by the heater, regardless of their velocity. In fact, we can always choose the proper amount of *power per phonon* ($E_{\rm ph}/t_{\rm MCS}$) in order to satisfy the Stefan-Boltzmann equation for the total power emitted by the heater:

$$P_H = N_H(E_{\rm ph}/t_{\rm MCS}) = \sigma A_H T_H^4 \ . \tag{5.3}$$

Here N_H is the total number of phonons emitted by the heater during the simulation, A_H is the area of the heater, ϵ has been set equal to unity since the heater absorbs all incident phonons, and T_H is the absolute heater temperature. We need not worry about the phonons that are reabsorbed by the heater, since the temperature of the heater is only defined in terms of the number of phonons *emitted* from its surface (which is greater than the number absorbed, since the heater is not in thermal equilibrium with the rest of the crystal). Using the Stefan-Boltzmann equation for *any* other area element dS on the crystal surface, we can define a normalized, unitless temperature as

$$T_{dS,\rm norm}^4 \equiv \frac{T_{dS}^4}{T_H^4} = \frac{N_{dS}}{A_{dS}} \bigg/ \frac{N_H}{A_H} \ , \tag{5.4}$$

where N_{dS} is the total number of phonons emitted from dS during the simulation, regardless of the specularity or emissivity of dS. This equation implies that the temperature of the crystal surface at the base clamp is zero since it emits no phonons. This does not present a problem because the equations for radiative heat transfer are linear in T^4, and we can always add an isothermal baseline solution to our normalized temperature profile in the simulation, such that $T'^4 = T^4 + T_b^4$. The baseline solution represents a crystal in thermal equilibrium at temperature T_b which is not conducting any heat. Here a comment about notation is in order. In Secs. III and IV, a capital T represented an absolute (not a relative) temperature, and a lower case t represented a relative and unitless temperature, obtained by linearizing in the presence of a large base temperature T_b. In this section, T'^4 stands for an absolute temperature, and T^4 is a relative temperature, given by $T^4 = T'^4 - T_b^4$. If we integrate $T_{dS,\rm norm}^4$ over the surface of the crystal for distances between x and $x+dx$ from the left end of the crystal, we can produce the normalized temperature $T_{\rm norm}^4(x)$, which is equal [see Eq. (4.4)] to the *linearized* and normalized temperature $\Phi(x)$ used in Sec. IV:

$$T_{\rm norm}^4(x) = \Phi(x) \ . \tag{5.5}$$

Therefore our $T_{\rm norm}^4(x)$ profiles obtained from the Monte Carlo simulations always have the same shape as the actual temperature profiles in an experiment, once the temperature of the base of the crystal has been subtracted off from the experimental temperature profile.

D. Temperature profiles generated by the simulations

Using Eq. (5.4) to define a temperature in our Monte Carlo simulations, we can construct temperature profiles $T_{\rm norm}^4(x)$ for various sample geometries, and include quantitatively the effects of phonon scattering at both the free surfaces of the crystal, and from the attached thermometer clamps. First let us go back to the simple cylindrical geometry described in Sec. IV. Figure 10 shows temperature profiles obtained for a cylinder with grey ($f \leq 1$) walls that is heated at one end by a black cross sectional sheet of uniform temperature. The circles are the result of the Monte Carlo simulation, the lines are from the integral equations described in Sec. IV. The agreement is excellent. This agreement confirms that our Monte Carlo simulation, which employs a very simple algorithm, nevertheless contains all the necessary physics to accurately model a true physical system. In addition to there being finite temperature jumps at the ends of the cylinder, the temperature profile is also not linear for $f \neq 0,1$, but shows curving at either side due to a finite cylinder length.

The effects of attached thermometers on the temperature profile are easy to demonstrate with a Monte Carlo simulation. Figures 12(a) and 12(b) show temperature profiles for the sample geometries shown in Figs. 1(b) and 1(d), respectively. To obtain these profiles, the surface area of the crystal in the simulation is resolved into 0.5×0.5 mm^2 elements, and the number of phonons emitted during the simulation from each element is counted, in order to calculate a normalized temperature as given by Eq. (5.4). The temperatures of the elements on the sides of the crystal that are in contact with the clamps are then averaged laterally in order to improve statistics, and this produces the graphs in Figs. 12(a) and 12(b), which have a horizontal resolution of 0.5 mm.

Figure 12(a) shows how significant the scattering from attached thermometers can be. The temperature drop due to one of the large thermometer clamps is about equal to that accumulated between the clamps over a distance of 120 mm with $f=0.03$. In order to conduct experiments which are sensitive to small f's (i.e., high specularities), we must use smaller thermometer clamps and larger spacings between thermometer clamps. Figure 12(b) shows the result of reducing the area of the thermometer clamps by a factor of 15, and maintaining about the same clamp spacing. For $f=0$, the temperature difference ΔT is still determined solely by the diffuse scattering at the thermometer clamps. However, for $f=0.03$, the temperature drop at the thermometers is negligible compared to the drop due to the diffuse phonon scattering between the thermometers. Figure 12(b) illustrates the attainable sensitivity of our thermal conductance technique to small amounts of diffuse scattering at the crystal surfaces. Our technique can achieve greater sensitivity for small f's than single reflection phonon experiments because the phonons in our thermal conductance experiments undergo *many* reflections (and therefore many possible diffuse scattering events) while in transit between the two thermometers, and the measured temperature difference ΔT has summed the effects of these diffuse scattering events.

The additional curving of the temperature profiles shown in Fig. 12 right next to the heater and base clamps (i.e., 3 mm $< x <$ 7 mm and 139 mm $< x <$ 145 mm) is a real physical effect, not an artifact of the simulation.

Even though the heater is the source of all the phonons in the simulation, it is still a black surface, and phonons emitted from one part of its surface can be blocked (reabsorbed) by another part of its surface, before they can propagate down the length of the sample. Surface points very near the heater are "shaded" in this way more than other points, and actually receive a smaller heat flux. A similar explanation holds for the curving next to the base clamp.

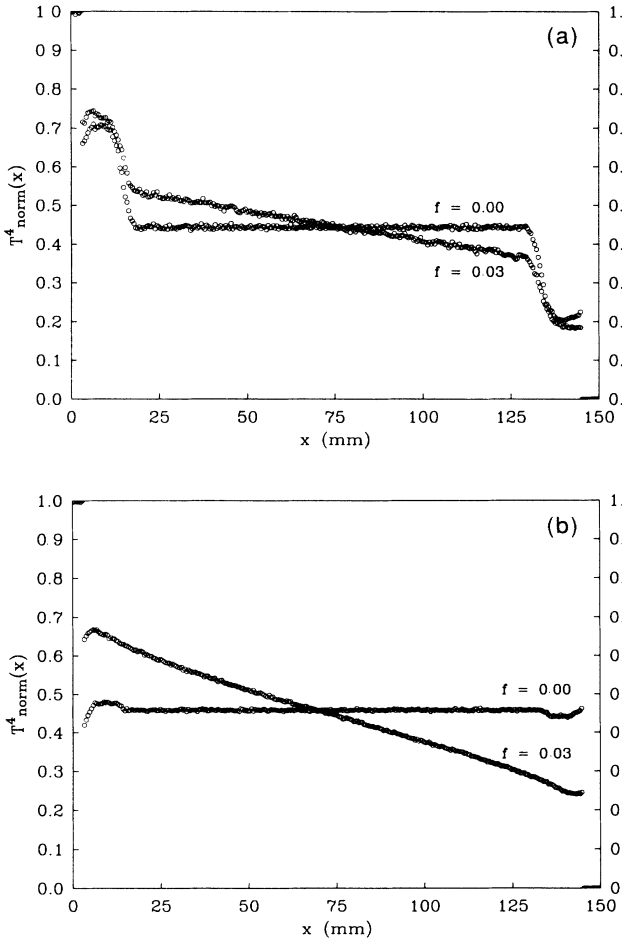

FIG. 12. Normalized temperature profiles for the geometries of Figs. 1(b) and 1(d), and for diffuse scattering probabilities $f=0.00$ and $f=0.03$ at the free surfaces of the crystal. In the simulations for these figures the thermometer clamps were made nonthermalizing, and were given a diffuse scattering fraction $f=1$. (a) The thermometer clamps have an area of 3 mm×5 mm and are centered at $x=14.5$ and 133.5 mm. This temperature profile shows how significant the scattering from attached thermometers can be. The temperature drop due to one of the large thermometer clamps is about equal to that accumulated between the clamps over a distance of 120 mm with $f=0.03$. (b) The thermometer clamps have an idea of 1 mm×1 mm and are centered at $x=13.5$ and 134.5 mm. The temperature drop due to phonon scattering at one of these small clamps is negligible when compared to that produced by phonon scattering at the free surfaces with $f=0.03$. This profile illustrates that the experiments which use small clamps are very sensitive to small amounts of diffuse scattering at the crystal surface.

E. Additional considerations for comparisons to experiment, and for determining *f*

In order to use our Monte Carlo simulations to determine the f present in our thermal conductance experiments, we must derive more than a normalized temperature profile from the simulations. We must determine the total phonon power conducted through the crystal in the simulation [which is not the same as the total power P_H emitted by the heater in Eq. (5.3), since some of the heater power is reabsorbed by the heater before leaving the crystal]. Then we can use the normalized profiles to calculate a phonon mean free path $\bar{l}_{\text{MCS}}$, which we can then compare to $\bar{l}_{\text{expt}}$. The total thermal power conducted through the crystal in the simulation is simply proportional to the number of phonons N_{exit} which left the crystal through the base clamp during the simulation:

$$\dot{Q}=N_{\text{exit}}(E_{\text{ph}}/t_{\text{MCS}}) , \tag{5.6}$$

where we have used the same $(E_{\text{ph}}/t_{\text{MCS}})$ factor as that used in Eq. (5.3), and for the same reason. The only relevant time scale is that of t_{MCS}. Phonons which are reabsorbed by the heater contribute nothing to the conducted power. In addition, the amount of time a phonon spends in the crystal before exiting at the base or being reabsorbed by the heater (i.e., its lifetime) does not affect the amount of power it conducts. This is clear because the future of a phonon emitted from the heater is not well predetermined, so that the rate at which potentially long-lived phonons are emitted from the heater is the same as the rate that potentially short-lived phonons are emitted. Furthermore, since thermal conductance is a *steady-state* measurement, the number of either long-lived or short-lived phonons in the crystal is constant with respect to time. Therefore, the long-lived phonons exit the base of the crystal at the same *rate* as the short lived ones; they have simply spent more time *in* the crystal. Hence all the phonons leaving the crystal at the base make the same contribution to the conducted power, *regardless of how long they took to exit.*

Let us also define a normalized power as

$$P_{\text{norm}} \equiv \frac{\dot{Q}}{P_H} = \frac{N_{\text{exit}}}{N_H} . \tag{5.7}$$

With this definition we can derive an expression (see Appendix A) for the phonon mean free path $\bar{l}_{\text{MCS}}$ which is obtained from the Monte Carlo simulations, and which directly corresponds to the $\bar{l}_{\text{expt}}$ measured in experiments:

$$\bar{l}_{\text{MCS}} = \frac{3}{4} \frac{\Delta x}{\Delta(T^4)_{\text{norm}}} \frac{A_H}{A} P_{\text{norm}} , \tag{5.8}$$

where $\Delta(T^4)_{\text{norm}} = T^4_{\text{warm,norm}} - T^4_{\text{cold,norm}}$ is the normalized temperature difference between the warm and cold thermometers as given by Eq. (5.4), and A is the cross-sectional area of the sample.

The beauty of Eq. (5.8) is that the only units which appear are those of length and area; hence $\bar{l}_{\text{MCS}}$ is only dependent on the geometry of the crystal in the simulation (and the chosen diffuse scattering probability f). As mentioned in the introduction, the $\bar{l}$ derived from thermal conductance experiments, as well as from our simulations, is not necessarily the average distance a phonon travels between diffuse scattering points. In fact, the simulations show that this is only true in the limit of an infinitely long sample with $f=1$ (i.e., the Casimir limit). For instance, if we apply Eq. (5.8) to the case of two parallel infinite black planes separated by a distance d (the model discussed in Sec. III), we obtain $\bar{l}=\frac{3}{4}d$ as the phonon mean free path which would be calculated from both the experiment and from the simulation, whereas the average path length between the two planes must be larger than d.

The statistical uncertainty in the temperature of each thermometer, as determined from the simulations, is inversely proportional to the square root of the total number of phonons emitted from its thermometer clamp. For geometries with small thermometer clamps, the simulation must emit a large number of phonons from the heater in order to produce a small statistical uncertainty in ΔT. The smooth profiles shown in Fig. 12(b) are the result of 6 000 000 phonons emitted from the heater. For the worst case of $f=0$, the statistical uncertainty in ΔT (and hence in $\bar{l}_{\mathrm{MCS}}$) is about 8%. Note that this uncertainty in $\bar{l}_{\mathrm{MCS}}$ is much larger than the corresponding uncertainty in the value of the diffuse scattering probability f determined from $\bar{l}_{\mathrm{MCS}}$. Simulations of this magnitude require a fast computer, and we are fortunate to be able to make use of the Cornell National Supercomputer Facility. Our simulations also require a very good random number generator. A great improvement can be made to a mediocre computer-supplied random number generator by first filling an array with these low quality random numbers, and then selecting a random element from that array to serve as a better random number. The empty slot in the array is refilled with another low quality random number. We used such an algorithm,[20] but found that the sequence of generated random numbers still contained non-negligible correlations, and was therefore insufficient to produce smooth temperature profiles for large f's. The next improvement was to refill the entire array after every 10 000th random number, using a seed number that was constantly incremented during the simulation. This additional improvement was enough to produce smooth temperature profiles.

In order to improve the accuracy of our results for $\bar{l}_{\mathrm{MCS}}$ obtained from Eq. (5.8), our simulations also take into account the effects of elastic anisotropy on heat conduction in the boundary scattering regime. In elastically anisotropic crystals, the phonon momentum vector **k** is not in general parallel to the direction of energy propagation given by the phonon group velocity vector **g**. Previous experimental and theoretical results for phonon focusing effects[21-25] demonstrate that the cosine distribution for a black surface applies to the distribution of emitted **g**, not of emitted **k**. When a phonon is emitted from a black or diffusely scattering surface, the Monte Carlo simulation first generates a random **k** *isotropically*, and then transforms this vector into the appropriate **g**. Next a rejection method[26] is used to modulate the resulting **g** distribution by $\cos\theta$, where θ is the angle between **g** and the surface normal. This modulation is carried out by generating a random number between 0 and 1 uniformly, and testing whether or not this number is smaller than $\cos\theta$. If the random number is smaller, then the phonon is emitted from the surface with direction **g**. If not, then another **k** is generated isotropically, and another attempt is made. The function **g**(**k**) depends on the elastic constants c_{11}, c_{12}, and c_{44} of the crystal.[27] In addition, when a phonon reflects specularly at a crystal surface, it is the perpendicular component of the momentum vector **k**, not the group velocity vector, which changes sign.[28] Therefore, the simulation first reflects **k**, and then recalculates **g**(**k**).

The results of our simulations showed that the addition of elastic anisotropy had only a small effect on the phonon mean free path for the crystallographic orientations of our Si samples ($\langle 111 \rangle$ along the length of the sample), which agrees with the findings of McCurdy *et al.*,[29] and also with our experimental results for rough samples. For a rough $\langle 111 \rangle$ sample of our geometry, the Monte Carlo simulations give an inverse phonon mean free path of $\bar{l}_{\mathrm{MCS}}^{-1}=2.15\ \mathrm{cm}^{-1}$, which compares very well with our experimental results of about $\bar{l}_{\mathrm{expt}}^{-1}=2.08\ \mathrm{cm}^{-1}$ between 50 mK and 1 K (see Fig. 3). We estimate our experimental accuracy to be about 5%.

F. Results for $f(T)$ of polished samples

To determine the f present in our experiments on polished samples, we first needed to determine the effective emissivity of the attached indium coated thermometer and base clamps. Appendix B describes how the clamp emissivity was determined from experiments and simulations for large clamp geometries. We found that $\epsilon_{\mathrm{clamps}}=0.40$. We then used this same $\epsilon_{\mathrm{clamps}}$ in our simulations of experiments with small thermometer clamps (also indium coated). These experiments are more sensitive to phonon scattering at the free surfaces of the crystal, giving more accurate determinations of f.

We now have everything that we need to make a *quantitative* comparison between the results of the Monte Carlo simulations and experiments for polished samples, and to confidently determine the effective diffuse scattering probability f for phonons at our polished silicon crystal surfaces. Figure 13 shows some of the inverse phonon mean free paths obtained from our simulations using Eq. (5.8), $\bar{l}_{\mathrm{MCS}}^{-1}(f)$, and also the temperature-dependent inverse phonon mean free paths obtained from experiments, $\bar{l}_{\mathrm{expt}}^{-1}(T)$, for the sample geometry shown in Fig. 1(d) (small clamps, distant spacing). The statistical uncertainties for $\bar{l}_{\mathrm{MCS}}$ are about 3%. This graph shows the sensitivity of $\bar{l}^{-1}$ to very small amounts of diffuse scattering at the crystal surface. This sensitivity allows us to determine very small diffuse scattering probabilities f, or very high specularities $(1-f)$, with great precision. Figure 14 shows the result of combining $\bar{l}_{\mathrm{MCS}}^{-1}(f)$ with $\bar{l}_{\mathrm{expt}}^{-1}(T)$ to produce $f(T)$ for the sample geometries of Figs. 1(c) and 1(d). This figure represents the final result of our investigation. We can see that our clean polished silicon surfaces are about 99.87±0.01% specular ($f=0.0013\pm0.0001$) at the lowest temperature in our

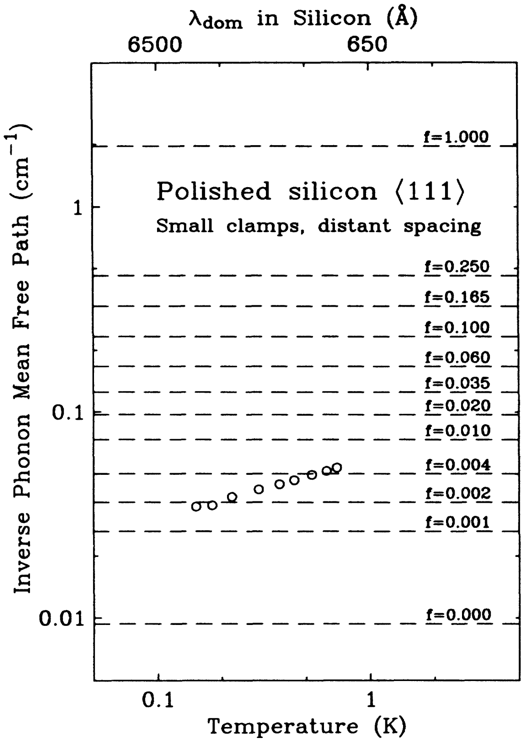

FIG. 13. The circles show the inverse phonon mean free path as a function of temperature as obtained from a thermal conductance experiment on a polished silicon sample with the geometry of Fig. 1(d) (small clamps, distant spacing). The horizontal dashed lines show the inverse phonon mean free path as a function of the diffuse scattering probability f, as determined by a Monte Carlo simulation of radiative heat transfer in the same sample geometry. This graph can be used to determine the effective f seen in experiments for polished samples as a function of temperature, for this sample geometry.

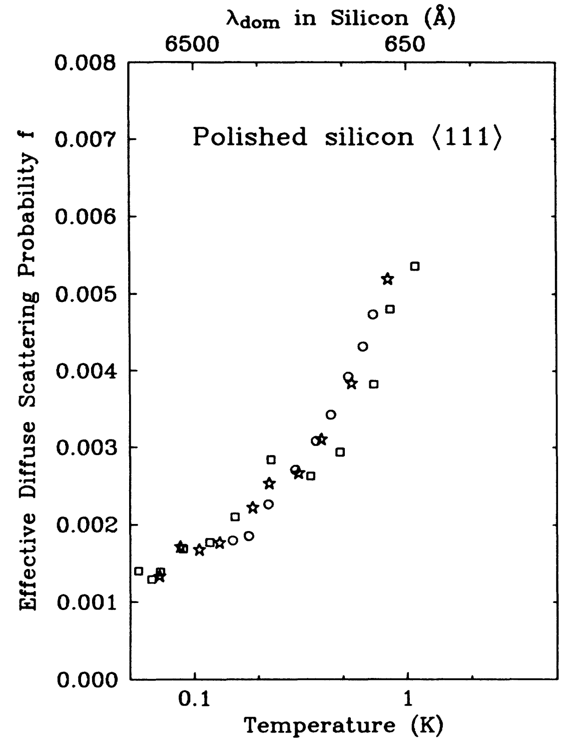

FIG. 14. The effective diffuse scattering probability f of phonons at a polished silicon crystal surface as a function of temperature for the sample geometries shown in Figs. 1(c) and 1(d). Open circles: small clamps, distant spacing; open squares and open stars: small clamps, close spacing. These curves were obtained by combining $\overline{l}^{\,-1}_{\rm expt}(T)$ and $\overline{l}^{\,-1}_{\rm MCS}(f)$ in a manner similar to that shown in Fig. 13. Note that the three curves agree within the experimental uncertainty, which should be the case, since the same polishing and cleaning procedures were used for both samples. The various possible systematic errors are discussed in the text.

experiments. Again, the high precision of our results for small f is due to the phonons experiencing many possible diffuse scattering events which can contribute to the measured ΔT between the two thermometers. Note that the $f(T)$ results for the small clamps, distant spacing geometry [Fig. 1(d)] are less noisy because of the greater sensitivity given by the distantly spaced clamps.

In spite of the excellent precision of our results for $f(T)$, their accuracy is limited by several possible sources of systematic error. These errors stem from a lack of experimental control, not from the statistical uncertainty of the Monte Carlo simulations. For instance, the Monte Carlo simulations showed that the measured phonon mean free path should depend slightly on which faces of the crystal the clamps are mounted on, i.e., the ⟨110⟩ or the ⟨211⟩ faces. This effect was discovered after the experiments were performed, and the faces of our samples were never identified. Another possible source of error arises from the preparation of the indium coated clamps. Although the surface conditions of all of the silicon samples were controlled by being subjected to the same cleaning procedure, the indium/silicon interface of the attached clamps was not well characterized. Since there is very little diffuse scattering at the crystal surfaces of polished samples at the lowest temperatures, $\overline{l}^{\,-1}_{\rm expt}$ is determined mostly by the scattering at the thermometer, heater and base clamps. At the time that the experiments were performed, we were not aware of how significant these effects could be. The indium coating on the small thermometer clamps had worn off a little bit, exposing some rough parts of the underlying cooper surface. Therefore the area of contact with the silicon sample was probably less than 1 mm^2. Taking these possible systematic errors into account, we estimate that our final results for the diffuse scattering probability at the lowest temperatures are uncertain by at most 25%. In spite of this uncertainty, the $f(T)$ results for the two different samples are nearly identical, suggesting that we were successful in controlling our surface conditions by adhering to a strict cleaning and polishing procedure. In future experiments we can take greater care to reduce the above possible systematic errors.

Although the silicon crystals used in our experiments were of exceptional purity, it is possible that there remained some bulk phonon scattering from energy level splittings in the electronic states of impurities. This is especially true for the rough boron-doped 0.5 cm×0.5 cm×5.0 cm samples, since boron impurities have been shown to product significant and temperature-dependent bulk phonon scattering in our temperature range.[30,31] We have performed measurements on *polished* boron-doped samples (not reported here, but in previous studies[2]), and found a strong temperature dependence to $\bar{l}^{-1}$, which could be as much as a factor of 2 larger than for our measurements on polished 0.5 cm×0.5 cm×15.0 cm phosphorus-doped samples. In order to accurately determine the amount of bulk scattering in either the boron-doped or the phosphorus-doped samples, we must perform measurements with their surfaces roughened, so that we know exactly what the contribution to $\bar{l}^{-1}$ is from surface scattering (assuming that it follows a cosine distribution). We have not yet performed these experiments for our phosphorous doped samples, but our $\bar{l}_{\text{expt}}^{-1}$ for rough *boron*-doped samples shows very little temperature dependence. Any observed temperature dependence in $\bar{l}_{\text{expt}}^{-1}$ would arise from a temperature dependence to the bulk scattering, since surface scattering from a rough surface should be temperature independent. The lack of any significant temperature dependence for the boron doped samples suggests that we probably do not have enough experimental precision to accurately determine the amount of bulk phonon scattering in our phosphorous doped samples. However, since our $\bar{l}^{-1}$ data for these polished samples decrease monotonically with decreasing temperature, we believe that the diffuse scattering seen in our temperature range is caused predominately by residual surface roughness, and not by bulk impurities. In either case, the scattering remaining at the lowest temperatures is quite small.

In support of this conclusion, note that the size of the silica particles used in the Syton polishing process for our samples is on the order of 400 Å. Assuming that the polishing process damages the surface with a feature size a little smaller than the size of the abrasive particles, we expect to see a large enhancement in f when the dominant phonon wavelength λ_{dom} becomes equal to or smaller than say ~200 Å. For silicon, $\lambda_{\text{dom}}=650$ Å at 1 K, and Fig. 14 shows that f begins to increase more rapidly just below this temperature. Our results for f near 1 K (~100 GHz) are in qualitative agreement with earlier studies using heat pulse and monochromatic phonon techniques (Eisenmenger[32] gives a good review of the literature). Although it may seem cumbersome to perform these Monte Carlo simulations in order to determine f from our experiments, similar simulations are required to analyze the data obtained in phonon reflection experiments using the other techniques. Our technique has the advantage of spanning a wider range in phonon frequencies by merely changing the ambient temperature of the crystal.

VI. CONCLUSIONS

We have compared results of low temperature thermal conductance measurements on pure single crystals of polished silicon with models of phonon blackbody radiation in simple geometries. These models have illustrated the physical origin of the sample geometry effects seen in the experiments. The thermal conductance was found to depend not only on the sample size, but also on the size and spacing of the attached thermometer clamps. Our Monte Carlo simulations are sophisticated enough to model the exact crystal geometry as well as to include the effects of elastic anisotropy, and have produced temperature profiles which demonstrate quantitatively the effects of thermometer clamps. These simulations have also allowed a quantitative comparison with the phonon mean free path obtained in experiments. This comparison has enabled us to calculate the diffuse scattering probability f of phonons at the polished silicon crystal surfaces as a function of temperature. We have obtained direct results for $f(T)$ in a phonon frequency range (5 to 100 GHz) which is not generally accessible using ultrasound, heat pulse, or superconducting tunnel junction techniques. Our results for $f(T)$ are quite reproducible for different data runs on the same sample. The absolute accuracy of our results is limited by the amount of detailed information known about the experimental sample geometry, not by the performance of the Monte Carlo simulations. Our results illustrate the usefulness of low-temperature thermal conductance measurements for investigating defects and adsorbates at crystal surfaces, and for studying more general geometry effects in radiative heat transfer.

Note added in proof. Some of the concepts discussed in this paper concerning phonon radiative heat transfer in polished crystals (including clamp-size effects) were also considered by K. M. Hayes [Ph.D. thesis, University of California at Irvine, 1985 (unpublished)].

ACKNOWLEDGMENTS

The authors thank R. E. Buxbaum, E. T. Swartz, N. S. Wingreen, J. P. Sethna and J. W. Wilkins for many helpful discussions. We also thank V. Narayanamurti for supplying the high purity silicon samples used in the experiments, and the employees of the AT&T Bell Laboratories Allentown Facility for polishing them. This work was supported by the National Science Foundation through the Cornell University Materials Science Center. The Monte Carlo simulations were conducted using the Cornell National Supercomputer Facility, a resource of the Center for Theory and Simulation in Science and Engineering at Cornell University, which is funded in part by the National Science Foundation, New York State, and the IBM Corporation.

APPENDIX A

In this appendix we derive the expression for $\bar{l}_{\text{MCS}}^{-1}$ which is used to compare the results of the Monte Carlo simulations with experiment. Substituting for P_H in Eq. (5.3) from Eq. (5.7), we obtain an equation for $\dot{Q}$:

$$\dot{Q}=\sigma A_H T_H^4 P_{\text{norm}} . \tag{A1}$$

We have identified the *microscopic* dynamics of the Monte Carlo simulation with those of a real experiment, and so conclude that the *macroscopic* quantities measured in experiments (such as thermal conductance) can also be derived from the simulation. Therefore we are at liberty to apply the same formulae to the simulation that are applied to thermal conductance measurements in the boundary scattering regime, such as

$$\Lambda = \tfrac{1}{3} C_v \bar{v} \bar{l} \,, \tag{2.4}$$

where $\bar{v}$ is given by Eq. (2.5). We can also make use of

$$\Lambda = \frac{\dot{Q}/A}{\Delta T/\Delta x} \,, \tag{2.1}$$

where A is the cross-sectional area of the sample, and ΔT is the temperature difference between the thermometers separated by a distance Δx in the simulation. The above two equations can be combined to give another equation for $\dot{Q}$:

$$\dot{Q} = \tfrac{1}{3} C_v \bar{v} \bar{l} A \frac{\Delta T}{\Delta x} \,. \tag{A2}$$

We can also rewrite Eq. (3.3) as

$$\sigma = \frac{1}{16} \frac{C_v \bar{v}}{T_H^3} \,, \tag{A3}$$

where C_v is the specific heat of the crystal at the heater temperature T_H. Eliminating $\dot{Q}$ from Eqs. (A1) and (A2), substituting Eq. (A3) for σ, and solving for $\bar{l}$, we have

$$\bar{l} = \frac{3}{16} \frac{\Delta x}{\Delta T} \frac{A_H}{A} T_H P_{\text{norm}} \,. \tag{A4}$$

This equation is not very accurate, however. We have chosen the specific heat C_v in Eq. (2.4) to be that of the crystal at the temperature of the heater, T_H. Recall that the base of the crystal in the simulation is at $T=0$, and that $C_v \propto T^3$. Therefore we have not chosen a good average specific heat. In a real experiment, the temperature of the base is nearly the same as the temperature of the heater, and a good average for C_v can be used in Eq. (2.4). We can do the same for our Monte Carlo simulations, as described below.

Let us imagine another Monte Carlo simulation for a crystal of the same geometry, but where there is no net heat flow through the crystal. All surface elements of the crystal are at the same temperature T_b, and have emitted the same number of phonons per unit area during the simulation. We can imagine that these extra phonons were also present in our previous simulation, and so we can add the two temperature profiles, such that

$$T_H'^4 \equiv T_H^4 + T_b^4 \,. \tag{A5}$$

We can also redefine

$$P'_{\text{norm}} \equiv \frac{\dot{Q}}{P'_H} = \frac{N_{\text{exit}}}{N_H + N_b} = P_{\text{norm}} \frac{T_H^4}{T_H'^4} \,, \tag{A6}$$

where N_b is the total number of phonons emitted from the heater for the isothermal crystal. All the phonons in the isothermal simulation are eventually reabsorbed by the heater; the base clamp is made nonabsorbing since there is no conducted power. Equation (A3) becomes

$$\sigma = \frac{1}{16} \frac{C_v \bar{v}}{T_H'^3} \,, \tag{A7}$$

where C_v is the specific heat at the new heater temperature T'_H. If T_b is large enough, then C_v is nearly the same throughout the crystal. The power conducted through the crystal remains the same since the isothermal simulation carries no heat, and can be expressed as [cf. Eq. (A1)]

$$\dot{Q} = \sigma A_H T_H'^4 P'_{\text{norm}} \,. \tag{A8}$$

Equation (2.1) is still valid, and so we can again make use of

$$\dot{Q} = \tfrac{1}{3} C_v \bar{v} \bar{l} A \frac{\Delta T}{\Delta x} \,. \tag{A2}$$

We eliminate $\dot{Q}$, using Eq. (A7) for σ, and then Eq. (A4) becomes

$$\bar{l} = \frac{3}{16} \frac{\Delta x}{\Delta T} \frac{A_H}{A} T'_H P'_{\text{norm}} \,. \tag{A9}$$

This formula, as compared to Eq. (A4), is accurate for $T'_H \gg \Delta T$.

However, we can simplify the above expression even further. In a thermal conductance experiment the measured temperature difference ΔT is usually about 1% of the average absolute temperature of the crystal. Since we are comparing our Monte Carlo results with such experiments, we can assume that $T'_H \gg \Delta T$. In fact, for simplicity, we will consider the limiting case of $\Delta T/T'_H \to 0$, and assume that this approximates the actual experimental situation. Therefore we write

$$\lim_{\Delta T/T'_H \to 0} \Delta T = \frac{\Delta(T^4)}{4 T_H'^3} \,. \tag{A10}$$

Substituting for ΔT in Eq. (A9), we obtain

$$\bar{l} = \frac{3}{4} \frac{\Delta x}{\Delta(T^4)} \frac{A_H}{A} T_H'^4 P'_{\text{norm}} \,.$$

We can then use the definition of P'_{norm} in Eq. (A6) to derive

$$\bar{l}_{\text{MCS}} = \frac{3}{4} \frac{\Delta x}{\Delta(T^4)_{\text{norm}}} \frac{A_H}{A} P_{\text{norm}} \,, \tag{5.8}$$

where

$$\Delta(T^4)_{\text{norm}} = T^4_{\text{warm,norm}} - T^4_{\text{cold,norm}}$$

is the normalized temperature difference between the two thermometers as given by Eq. (5.4). Note that this final equation for $\bar{l}_{\text{MCS}}$ does not depend on T_b, but only on our original normalized temperature profile.

APPENDIX B

To determine ϵ_{clamps} we performed thermal conductance measurements with two different thermometer clamp separations, each sample having large indium-coated thermometer clamps affixed as shown in Figs. 1(a) and 1(b). From previous experiments and simulations, we knew that the phonon scattering at these clamps was the predominant cause of the measured temperature difference between the two thermometers mounted on highly polished samples, i.e., that $\bar{l}$ was relatively insensitive to a few percent of diffuse scattering at the rest of the crystal surface [as shown in Fig. 12(a)]. For self-consistent results, we needed that the diffuse scattering probability $f=0.002$ for the free surfaces of the crystals in the simulations, and that $\epsilon_{\text{clamps}}=0.40$, in order to match both experiments. In other words, our experiments show that only 40% of the phonons incident on a surface in contact with a clamp are transmitted into that clamp.

In addition, we have attempted to calculate an average transmission coefficient of phonons from silicon to indium at a smooth interface by using acoustic mismatch theory for an isotropic medium.[33] We use an average sound velocity for silicon given by

$$\frac{1}{v_{\text{av}}^2}=\frac{1}{3}\sum_{i=1}^{3}\frac{1}{v_i^2}\,, \tag{B1}$$

where v_i is the sound velocity for the ith phonon mode in the silicon. Since the number of phonons of a given mode which strike an interface is proportional to their density of states times their velocity, we should weight the transmission coefficient of each mode by $1/v_i^2$ in order to determine an average transmission coefficient:

$$\frac{\Gamma_{\text{av}}}{v_{\text{av}}^2}=\frac{1}{3}\sum_{i=1}^{3}\frac{\Gamma_i}{v_i^2}\,, \tag{B2}$$

where the Γ_i are the transmission coefficients for the three phonon modes in the silicon as averaged over a cosine distribution $(0<\Gamma_i<1)$. Now we can easily calculate Γ_{av} by using tabulated values for transmission coefficients as given by Cheeke *et al.*[33] We find that $\Gamma_{\text{av}}=0.84$. Although this approach is somewhat arbitrary, it is difficult to decide how to best define an average transmission coefficient which can be compared to the effective emissivity of our thermometer clamps as determined by the Monte Carlo simulations, since we have not recorded the angular distribution of phonons *incident* on our clamps in the simulations. Furthermore, the calculations by Cheeke *et al.* do not take into account the effects of elastic anisotropy, whereas our simulations do. Nevertheless, by comparing the experimental phonon transmission coefficient from silicon to the indium coated clamps ($\epsilon_{\text{clamps}}=0.40$) with the theoretical Si→In transmission coefficient ($\Gamma_{\text{av}}=0.84$), we see that the measured phonon transmission coefficient is only 0.40/0.84=48% of what is expected, possibly due to poor mechanical contact on the atomic scale. This result is in agreement with our measurements of the thermal boundary resistance between these indium-coated clamps and polished silicon samples: We found that at 52 mK the measured thermal boundary resistance was 2.16 times larger than expected from acoustic mismatch theory, or equivalently that the measured average transmission coefficient was only 1/2.16=46% of the ideal.

---

[1] H. B. G. Casimir, Physica **5**, 495 (1938).

[2] Tom Klitsner and R. O. Pohl, Phys. Rev. B **36**, 6551 (1987); **34**, 6045 (1986).

[3] A good review of these techniques is given by W. Eisenmenger, in *Phonon Scattering in Condensed Mattei V,* edited by A. C. Anderson and J. P. Wolfe (Springer-Verlag, Berlin, 1986), p. 204. The highest phonon frequencies yet achieved with ultrasonic transducers (those which can transmit phonons into a variety of substrates) are on the order of 10 GHz—see A. Ambrosy, K. Holdik, W. Scheitler and H. Schulze, in *Phonon Scattering in Condensed Matter,* edited by W. Eisenmenger *et al.* (Springer-Verlag, Berlin, 1984), p. 61. Higher frequency coherent phonons (up to 35 GHz) have been generated in piezoelectric crystals using movable hypersound beams—see O. Weis, in *Phonon Scattering in Condensed Matter V,* edited by A. C. Anderson and J. P. Wolfe (Springer-Verlag, Berlin, 1986), p. 381. An up to date description of the single reflection heat pulse technique using a superconducting bolometer is given by R. Maboudian, C. Carraro, D. L. Goodstein, R. M. Housley, and T. A. Tombrello (unpublished). Recent descriptions of the applications of superconducting tunnel junctions for the generation and detection of monochromatic phonons are given by H. Kinder, in *Physics of Phonons,* edited by T. Paszkiewicz (Springer-Verlag, Berlin, 1987), p. 289, and by W. Dietsche, in *Phonon Scattering in Condensed Matter V,* edited by A. C. Anderson and J. P. Wolfe (Springer-Verlag, Berlin, 1986), p. 366. An earlier but more comprehensive review of superconducting tunnel junctions is given by H. Kinder, in *Nonequilibrium Phonon Dynamics,* Vol. 124 of *NATO Advanced Study Institute, Series B: Physics,* edited by W. E. Bron (Plenum, New York, 1985), p. 129.

[4] A comprehensive review of phonon generation and detection using electronic states of impurities is given by W. Bron, in *Nonequilibrium Phonons in Nonmetallic Crystals,* edited by W. Eisenmenger and A. A. Kaplyanskii (North-Holland, Amsterdam, 1986), p. 227. Also in the same book, see the two chapters on detection of high frequency phonons by phonon-induced fluorescence by K. F. Renk on pages 277 and 317. Renk gives another recent review of related phonon pulse techniques in *Excited-State Spectroscopy in Solids,* Proceedings of the International School of Physics "Enrico Fermi," Course 96, Varenna, Italy, edited by U. M. Grassano and N. Terzi (North-Holland, Amsterdam, 1987), p. 213. The techniques mentioned above have been used to study phonon reflection coefficients in some cases. For example, indirect determinations of $f(\omega)$ at frequencies below 100 GHz have been made using a spin-phonon-spectrometer technique. However, this technique is limited to optically transparent crystals containing special magnetic impurities—see C. H. Anderson and E. S. Sabisky, Phys. Acoust. **8**, 1 (1971); also E. S. Sabisky and C. H. Anderson, Solid State Commun. **17**, 1095 (1975). The technique of stimulated Brillouin scattering has been used to measure the reflection coefficient of 24.8-GHz phonons in quartz. Again, this technique is only applicable to transparent crystals, and the phonon frequency is not

easily tunable—see G. Schubert, P. Leiderer and H. Kinder, J. Low Temp. Phys. **39**, 363 (1980).

[5] See, for example, M. N. Ozisik, *Radiative Transfer* (Wiley-Interscience, New York, 1973).

[6] A. K. Raychaudhuri, Ph.D. thesis, Cornell University, 1980 (unpublished).

[7] Tom Klitsner, Ph.D. thesis, Cornell University, 1986 (unpublished).

[8] C. Kittel, *Introduction to Solid State Physics,* 5th ed. (Wiley, New York, 1976), p. 143.

[9] J. M. Ziman, *Electrons and Phonons* (Oxford University Press, London, 1962), pp. 257ff.

[10] H. Beck, in *Dynamical Properties of Solids,* edited by G. K. Horton and A. A. Maradudin (North-Holland, Amsterdam, 1975), p. 205.

[11] W. S. Hurst and D. R. Frankl, Phys. Rev. B **186**, 801 (1969).

[12] J. M. Ziman, *Electrons and Phonons,* Ref. 9, pp. 460–465.

[13] R. Berman, F. E. Simon and J. M. Ziman, Proc. R. Soc. London, Ser. A **220**, 171 (1953).

[14] C. G. Eddison and M. N. Wybourne, J. Phys. C **18**, 5225 (1985).

[15] M. Perlmutter and R. Siegel, J. Heat Transfer **85C**, 55 (1963).

[16] J. E. VanCleve, T. Klitsner, and R. O. Pohl, in *Phonon Scattering in Condensed Matter V,* Ref. 3, p. 177.

[17] F. Reif, *Fundamentals of Statistical and Thermal Physics* (McGraw-Hill, New York, 1965), p. 385.

[18] R. W. Pohl, *Optik und Atomphysik* (Springer-Verlag, Berlin, 1954), p. 168.

[19] There is experimental evidence that some *inelastic* scattering of phonons takes place at rough crystal surfaces. See L. J. Challis, S. V. J. Kenmuir, A. P. Heraud, and P. A. Russell, in *Phonon Scattering in Condensed Matter V,* Ref. 3, p. 180. However, this partial thermalization can be treated as diffuse scattering in the Monte Carlo simulations.

[20] W. H. Press, B. P. Flannery, S. A. Teukolsky, and W. T. Vetterling, *Numerical Recipies* (Cambridge University Press, New York, 1986), p. 194.

[21] For a recent review, see H. J. Maris, in *Nonequilibrium Phonons in Nonmetallic Crystals,* edited by W. Eisenmenger and A. A. Kaplyanskii (North-Holland, Amsterdam, 1986), p. 51.

[22] B. Taylor, H. J. Maris and C. Elbaum, Phys. Rev. Lett. **23**, 416 (1969).

[23] G. A. Northrop and J. P. Wolfe, Phys. Rev. Lett. **43**, 1424 (1979).

[24] D. Marx and W. Eisenmenger, Z. Phys. B **48**, 277 (1982).

[25] A. K. McCurdy, Phys. Rev. B **26**, 6971 (1982).

[26] W. H. Press, B. P. Flannery, S. A. Teukolsky and W. T. Vetterling, *Numerical Recipies,* Ref. 20, p. 203.

[27] B. Taylor, H. J. Maris, and C. Elbaum, Phys. Rev. B **3**, 1462 (1971).

[28] B. A. Auld, *Acoustic Fields and Waves in Solids* (Wiley, New York, 1973), Vol. 2, pp. 6ff.

[29] A. K. McCurdy, H. J. Maris, and C. Elbaum, Phys. Rev. B **2**, 4077 (1970).

[30] A. Ambrosy, K. Lassmann, A. M. de Goër, B. Salce, and H. Zeile, *Phonon Scattering in Condensed Matter* (Springer-Verlag, Berlin, 1984), p. 361.

[31] A. M. de Goër, M. Locatelli, and K. Lassmann, J. Phys. (Paris), Colloq. **42**, C6-235 (1981).

[32] W. Eisenmenger, in *Phonon Scattering in Condensed Matter V,* Ref. 3, p. 204.

[33] J. D. N. Cheeke, H. Ettinger, and B. Hebral, Can. J. Phys. **54**, 1749 (1976).

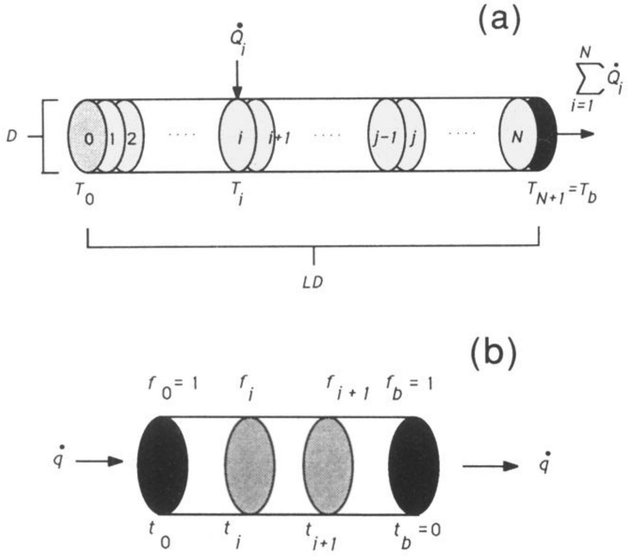

FIG. 5. (a) A one-dimensional model for radiative heat transfer. Each element of the sample surface, including the clamped area, is represented by a thermalizing sheet perpendicular to an otherwise specular tube of cross-sectional area A, which absorbs a fraction f_i of the radiation passing through it. All the heat leaves through the rightmost element, which represents the point at which the sample is clamped to the cryostat. (b) Reduced model of 1D heat transfer, for calculating the temperature drop between elements i and $i+1$ of the model shown in (a). By iteration, the entire solution may be obtained.

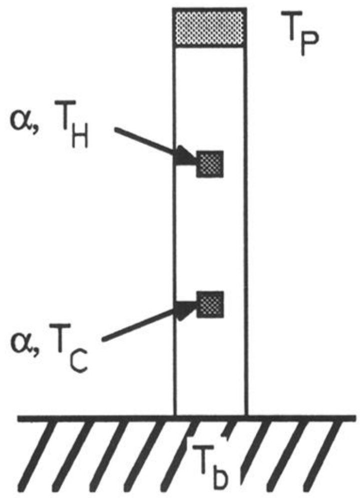

FIG. 6. Typical locations of heaters, thermometer clamps, and the base heat sink on a sample. The two-heater method of measuring thermal conductance puts in heat at H or C and measures T_P. The two-thermometer method puts in heat at P and measures T_H and T_C. The shaded squares at H and C represent the area under a clamp, which scatters phonons much more strongly than the clean surface. A fraction α of the phonons passing down the sample are scattered diffusely at the clamps.